



Eddington Envelopes: The Fate of Stars on Parabolic Orbits Tidally Disrupted by Supermassive Black Holes

Daniel J. Price¹ , David Liptai¹ , Ilya Mandel^{1,2,3} , Joanna Shepherd¹ , Giuseppe Lodato⁴ , and Yuri Levin^{1,5,6}

¹ School of Physics and Astronomy, Monash University, Clayton, VIC 3800, Australia; daniel.price@monash.edu

² The ARC Centre of Excellence for Gravitational Wave Discovery—OzGrav, Australia

³ Birmingham Institute for Gravitational Wave Astronomy and School of Physics and Astronomy, University of Birmingham, B15 2TT, Birmingham, UK

⁴ Dipartimento di Fisica, Università Degli Studi di Milano, Via Celoria 16, Milano 20133, Italy

⁵ Center for Theoretical Physics, Department of Physics, Columbia University, New York, NY 10027, USA

⁶ Center for Computational Astrophysics, Flatiron Institute, New York, NY 10010, USA

Received 2024 April 12; revised 2024 July 9; accepted 2024 July 9; published 2024 August 20

Abstract

Stars falling too close to massive black holes in the centers of galaxies can be torn apart by the strong tidal forces. Simulating the subsequent feeding of the black hole with disrupted material has proved challenging because of the range of timescales involved. Here we report a set of simulations that capture the relativistic disruption of the star, followed by 1 yr of evolution of the returning debris stream. These reveal the formation of an expanding asymmetric bubble of material extending to hundreds of au—an outflowing Eddington envelope with an optically thick inner region. Such outflows have been hypothesized as the reprocessing layer needed to explain optical/UV emission in tidal disruption events but never produced self-consistently in a simulation. Our model broadly matches the observed light curves with low temperatures, faint luminosities, and line widths of 10,000–20,000 km s^{−1}.

Unified Astronomy Thesaurus concepts: Tidal disruption (1696); Transient sources (1851); X-ray transient sources (1852); Supermassive black holes (1663); Black hole physics (159); Ultraviolet transient sources (1854); Active galactic nuclei (16); High energy astrophysics (739); General relativity (641)

Materials only available in the online version of record: animations

1. Introduction

In the classical picture of tidal disruption events (TDEs), the debris from the tidal disruption of a star on a parabolic orbit by a supermassive black hole (SMBH) rapidly circularizes to form an accretion disk via relativistic apsidal precession (Rees 1988). The predicted mass return rate of debris (Phinney 1989) is $\propto t^{-5/3}$, and the lightcurve is assumed to be powered by accretion and to follow the same decay.

This picture alone does not predict several properties of observed TDEs, mainly related to their puzzling optical emission (van Velzen et al. 2011, 2021; van Velzen 2018). These properties include (i) low peak bolometric luminosities (Chornock et al. 2014) of $\sim 10^{44}$ erg s^{−1}, $\sim 1\%$ of the value expected from radiatively efficient accretion (Svirski et al. 2017); (ii) low temperatures, more consistent with the photosphere of a B-type star than with that of an accretion disk at a few tens of gravitational radii ($R_g \equiv GM_{\text{BH}}/c^2$; Gezari et al. 2012; Miller 2015), and consequently large emission radii, ~ 10 – 100 au for a $10^6 M_\odot$ black hole (Guillochon et al. 2014; Metzger & Stone 2016); and (iii) spectral line widths implying gas velocities of $\sim 10^4$ km s^{−1}, much lower than expected from an accretion disk (Arcavi et al. 2014; Leloudas et al. 2019; Nicholl et al. 2019).

As a consequence, numerous authors have proposed alternative mechanisms for powering the TDE lightcurve, via either shocks from tidal stream collisions during disk formation (Lodato 2012; Piran et al. 2015; Svirski et al. 2017; Huang

et al. 2023; Ryu et al. 2023) or the reprocessing of photons through large-scale optically thick layers, referred to as Eddington envelopes (Loeb & Ulmer 1997), super-Eddington outflows (Strubbe & Quataert 2009), quasi-static or cooling TDE envelopes (Coughlin & Begelman 2014; Roth et al. 2016; Metzger 2022), or mass-loaded outflows (Jiang et al. 2016; Metzger & Stone 2016). Recent spectropolarimetric observations suggest reprocessing in an outflowing, quasi-spherical envelope (Patra et al. 2022).

The wider problem is that few calculations exist that follow the debris from disruption to fallback for a parabolic orbit with the correct mass ratio. The challenge is to evolve a main-sequence star on a parabolic orbit around an SMBH from disruption and to follow the subsequent accretion of material (Metzger & Stone 2016). The dynamic range involved when a $1 M_\odot$ star on a parabolic orbit is tidally disrupted by a $10^6 M_\odot$ SMBH is greater than 4 orders of magnitude: the tidal disruption radius is 50 times the gravitational radius, where general relativistic effects are important, while the apoapsis of even the most bound material is another factor of 200 further away. This challenge led previous studies to consider a variety of simplifications (Stone et al. 2019): (i) reducing the mass ratio between the star and the black hole by considering intermediate-mass black holes (Ramirez-Ruiz & Rosswog 2009; Guillochon et al. 2014); (ii) using a Newtonian gravitational potential (Evans & Kochanek 1989; Rosswog et al. 2008; Guillochon et al. 2009; Lodato et al. 2009; Golightly et al. 2019) or pseudo-Newtonian (Hayasaki et al. 2013; Bonnerot et al. 2016) or post-Newtonian approximations (Ayal et al. 2000; Hayasaki et al. 2016); (iii) simulating only the first passage of the star (Evans & Kochanek 1989; Khokhlov et al. 1993; Laguna et al. 1993; Frolov et al. 1994; Diener et al. 1997;



Original content from this work may be used under the terms of the [Creative Commons Attribution 4.0 licence](https://creativecommons.org/licenses/by/4.0/). Any further distribution of this work must maintain attribution to the author(s) and the title of the work, journal citation and DOI.

Kobayashi et al. 2004; Guillochon et al. 2009; Guillochon & Ramirez-Ruiz 2013; Tejeda et al. 2017; Gafton & Ross-wog 2019; Goicovic et al. 2019); and (iv) assuming stars initially on bound, highly eccentric orbits instead of parabolic orbits (Hayasaki et al. 2013, 2016; Bonnerot et al. 2016; Sadowski et al. 2016; Liptai et al. 2019; Hu et al. 2024).

These studies have, nevertheless, provided useful insights into the details of the tidal disruption process. In particular, it has been shown that the distribution of orbital energies of the debris following the initial disruption is roughly consistent with $dM/dE = \text{const}$, consistent with the analytic prediction of a $\propto t^{-5/3}$ mass fallback rate, although the details can depend on many factors, such as stellar spin, stellar composition, penetration factor, and black hole spin (Lodato et al. 2009; Kesden 2012; Guillochon & Ramirez-Ruiz 2013; Golightly et al. 2019; Sacchi & Lodato 2019). The importance of general relativistic effects in circularizing debris has also been demonstrated. The self-intersection of the debris stream, which efficiently dissipates large amounts of orbital energy, is made possible by relativistic apsidal precession (Bonnerot et al. 2016; Hayasaki et al. 2016; Liptai et al. 2019; Calderón et al. 2024). But until recently, debris circularization has only been shown for stars on bound orbits, with correspondingly small apoapsis distances and often deep penetration factors (we define the penetration factor as $\beta \equiv R_t/R_p$, where $R_t = R_*(M_{\text{BH}}/M_*)^{1/3}$ is the tidal radius and R_p is the pericenter distance).

Recent works have shown that circularization and initiation of accretion *is* possible in the parabolic case by a combination of energy dissipation in the “nozzle shock” that occurs on second pericenter passage (Steinberg & Stone 2024; but see Bonnerot & Lu 2022 and Appendix E for convergence studies of the nozzle shock) and/or relativistic precession leading to stream collisions (Andalman et al. 2022).

In this Letter, we present a set of simulations that self-consistently evolve a $1 M_\odot$ polytropic star on a parabolic orbit around a $10^6 M_\odot$ black hole from the star’s disruption to circularization of the returning debris and then accretion. We follow the debris evolution for 1 yr postdisruption, enabling us to approximately compute synthetic lightcurves that appear to match the key features of the observations.

2. Methods

We modeled the disruption of stars with mass $M_* = 1 M_\odot$ and radius $R_* = 1 R_\odot$ by an SMBH with mass $M_{\text{BH}} = 10^6 M_\odot$ using the general relativistic implementation of the smoothed particle hydrodynamics (SPH) code PHANTOM (Price et al. 2018) as described in Liptai & Price (2019).

We used the Kerr metric (Kerr 1963) in Boyer–Lindquist coordinates with the black hole spin vector along the z -axis and, unless otherwise specified, assumed an adiabatic equation of state for the gas with $\gamma = 5/3$. We deleted particles that fall within a radius of $R_{\text{acc}} = 5R_g$ (within the innermost stable circular orbit of a nonspinning black hole) from the simulation to avoid small time steps close to the horizon.

We placed the star on a parabolic orbit initially at a distance of $r_0 = 10R_t$ with velocity $v_0 = \sqrt{2GM_{\text{BH}}/r_0}$, where R_t is the tidal radius. The parabolic trajectory was oriented such that the star travels counterclockwise in the x – y plane and the Newtonian pericenter R_p was located on the negative y -axis. For inclined trajectories, we rotated the initial position and velocity vectors by an angle θ about the y -axis.

We modeled the star as a polytropic sphere with polytropic index $n = 3/2$ using 4,188,898 equal-mass particles at our highest resolution and approximately 512K particles in our medium-resolution calculations (real stars are expected to be more concentrated, which may alter the fallback rate, delaying the peak with respect to a polytropic model; e.g., Law-Smith et al. 2019), and we include the perturbation in the metric due to Newtonian self-gravity in our simulations to hold the star together during the predisruption phase.

For our main simulations, we employed an adiabatic approximation, implying that energy is trapped or advected rather than radiated. Appendix A reports a set of isentropic calculations where we assume shock heating to be immediately radiated away. The adiabatic simulations capture all accretion feedback down to $5R_g$, inside which particles are assumed to accrete without radiating.

Our point of closest approach is typically smaller than the Newtonian pericenter R_p due to relativity, and thus the “true” penetration factor is larger (by up to ~ 1 in our $\beta = 5$ calculation, where the true β is closer to 6).

2.1. Synthetic Lightcurves

We computed synthetic lightcurves, optically thick visualizations, and spectra from our models by solving the equation of radiative transfer in the form

$$\frac{dI_\nu}{d\tau} = S_\nu - I_\nu, \quad (1)$$

where $I_\nu \equiv I(\nu)$ is the intensity, τ is the optical depth, and ν is the frequency. For simplicity, we assumed local thermodynamic equilibrium such that $S_\nu \equiv B_\nu$, where $B_\nu = 2h\nu^3 c^{-2} \exp[h\nu/(k_B T) - 1]^{-1}$ is the Planck function. We also neglected time-dependent and general relativistic effects and special relativistic corrections to the shape of the photosphere (Abramowicz et al. 1991). That is, we considered rays to travel in a straight line to the observer. We solved for the optical depth using

$$d\tau = \frac{\nu_0}{\nu} \kappa \rho dz' = \gamma(1 - \beta_z) \kappa \rho dz'_0, \quad (2)$$

where $\beta_z \equiv v_z/c$, $\gamma = 1/\sqrt{1 - v^2/c^2}$, and ρ is the density in the rest frame of the fluid. The correction factor $\nu_0/\nu \equiv \gamma(1 - \beta_z)$ accounts for the optical depth change caused by the moving photosphere (Abramowicz et al. 1991; Ogura & Fukue 2013). We also computed B_ν in the observer’s frame (i.e., using $\nu = \gamma(1 + \beta_z)\nu_0$), accounting for the Doppler shift due to the motion of the photosphere.

We found the relativistic corrections to the optical depth to be negligible in practice (because our typical $v/c \lesssim 1/30$), giving a 1%–2% correction to the total luminosity. This also justifies our neglect of photospheric shape distortions. Potentially more significant is the difference between the “thermalization surface” and the photosphere in scattering-dominated flows (Abramowicz et al. 1991; Ogura & Fukue 2013). Full treatment of this issue is beyond the scope of our Letter (requiring a full 3D solution of the radiative transfer problem including scattering) but implies that we may underestimate the true temperature at the photosphere.

To compute the temperature from the specific internal energy, u , from the SPH calculation, we assumed gas and

radiation to be locally in equilibrium, giving

$$f(T) = \frac{3}{2} \frac{k_B T}{\mu m_H} + \frac{a T^4}{\rho} - u = 0, \quad (3)$$

where $\mu = 0.6$ is the mean molecular weight and a is the radiation constant. We solved this for each particle via Newton–Raphson iteration until $\Delta T/T_0 < 10^{-8}$, where the initial guess $T_0 = \min \left[\frac{2}{3} u (\mu m_H / k_B), (\rho u / a)^{1/4} \right]$.

We adopted the opacity prescription from Matsumoto & Metzger (2022; see their Figure 3 for a comparison to OPAL tables), where

$$\kappa = \kappa_{\text{mol}} + \kappa_e + (\kappa_H^{-1} + \kappa_K^{-1})^{-1}, \quad (4)$$

which includes molecular opacity $\kappa_{\text{mol}} = 0.1 Z \text{ cm}^2 \text{ g}^{-1}$, where $Z = 0.014$ is the metallicity; H^- opacity $\kappa_H = 1.1 \times 10^{-25} Z^{0.5} \rho^{0.5} T^{7.7} \text{ cm}^2 \text{ g}^{-1}$; bound–free and free–free opacity via Kramer’s law $\kappa_K = 1.2 \times 10^{26} Z(1+X) \rho T^{-7/2} \text{ cm}^2 \text{ g}^{-1}$ with $X = 0.698$ (both formulae assuming ρ in g cm^{-3} and T in K); and electron scattering $\kappa_e = \sigma_e n_e / \rho$, where $\sigma_e = 6.652 \times 10^{-25} \text{ cm}^2$ is the Thomson cross section. We computed n_e by solving for the hydrogen ionization fraction, $x = n_e / n_H$, from the Saha equation (assuming H only for simplicity) by solving the quadratic

$$\frac{x^2}{1-x} = \frac{1}{n_H} \left(\frac{2\pi m_e k_B T}{h^2} \right)^{3/2} \exp \left[-\frac{13.6 \text{ eV}}{k_B T} \right], \quad (5)$$

where $n_H = \rho / m_H$ is the hydrogen number density. In the limit of full ionization, this gives $\kappa_e = 0.4 \text{ cm}^2 \text{ g}^{-1}$. The main effect of Equation (5) is to make regions with $T \lesssim 10^4 \text{ K}$ transparent. In practice, we found identical results with $\kappa = \kappa_e$, since electron scattering dominates the opacity at our typical photospheric densities ($\sim 10^{-14} \text{ g cm}^{-3}$) and temperatures ($\sim 10^4 \text{ K}$).

We assumed a grid of pixels in the image plane with one ray per pixel, integrating front to back, each pixel containing 128 frequency bins spaced evenly in $\log_{10} \nu$ between 10^8 and 10^{22} Hz . A caveat is that Equation (4) assumes gray opacities, but we add blackbody spectra in a frequency-dependent manner. This is irrelevant anyway, since the dominant opacity is gray. Since our data consist of SPH particles, we performed the ray trace by sorting the particles by z' (the line of sight toward the observer, not necessarily the original z), considering the propagation of the ray bundle in turn through each particle, computing the optical depth integral (Equation (2)) through each particle using the smoothing kernel as described in Price (2007). We thus obtained a map of I_ν on our grid of pixels at 128 different frequencies. To “observe” the flow from different lines of sight, we simply rotated the particle distribution around the x -, y -, or z -axes while keeping the location of the observer fixed at $z' = \infty$ in the rotated coordinates (x' , y' , and z'). At early times, the photosphere can be unresolved by the SPH particles (e.g., Hatfull et al. 2021). To check for this, we flagged pixels in our synthetic images where a single particle contributed more than $d\tau > 1/3$ while $\tau < 1$. We then set a criterion on the unresolved area compared to the total area where $\tau > 1$. When $>1\%$ of pixels in the photosphere are poorly resolved, we show the lightcurve using semitransparent lines.

Synthetic spectral energy distributions were computed by integrating over all pixels in the image. Inferred bolometric luminosities were then computed by integrating the blackbody spectrum fitted to the optical band. To test our procedure, we confirmed that imaging a $1 R_\odot$ sphere of gas modeled with each particle given a uniform temperature $T = 5772 \text{ K}$ and a constant opacity produced a luminosity equal to the solar luminosity.

3. Results

Figure 1 shows snapshots of the long-term debris evolution in the $\beta = 1$, high-resolution, adiabatic simulation with a nonrotating black hole. The star takes approximately 7 hr to reach pericenter, at which point it is tidally disrupted and forms a long, thin debris stream. Approximately half of the stream is bound to the black hole, while the other half is unbound (visible as the thin, dense upward stream in the figure). The head of the stream (i.e., the most bound material) takes ~ 26 days to return to pericenter. After the stream passes through pericenter for a second time, the small amount of apsidal precession leads to stream self-intersection at the “outer shock” (most evident in inset panels shown at 60 and 90 days; see Appendix B for more detail on the outer shock), which causes material to eventually fall toward the black hole, driving the formation of kinetic outflows that spread almost isotropically, eventually encasing the black hole (main panel). A fraction of the material joins the returning debris and returns to pericenter; however, most of it goes into a low-density mechanical outflow. Following the fallback for 1 yr postdisruption, we find that the bubble continues to expand, with only a small amount of material forming an eccentric disk (lower panels of Figure 1). The large-scale debris structure (main panel) is similar to the “Eddington envelope” first proposed by Loeb & Ulmer (1997) except that ours is outflowing rather than static, as predicted by subsequent authors (Strubbe & Quataert 2009; Jiang et al. 2016; Metzger & Stone 2016).

Figure 2 shows the density (top), temperature (middle), and radial velocity (bottom) distributions of particles a year after disruption, with temperature calculated from Equation (3). The density of the outflowing envelope is $\sim 10^{-16} \text{ g cm}^{-3}$, approximately 6 orders of magnitude lower than the density of the stream, which is $\sim 10^{-10} \text{ g cm}^{-3}$. The typical outflow velocity is $\sim 10^4 \text{ km s}^{-1}$. After 1 yr, approximately 67% ($0.67 M_\odot$) of the stellar mass is in the incoming or unbound stream, 31.2% ($0.31 M_\odot$) in the envelope, and 0.8% ($0.008 M_\odot$) in the eccentric disk, while 1% ($0.01 M_\odot$) has been accreted by the black hole.

The top panel of Figure 3 shows the energy dissipation rate in our simulation, L_{shock} . This was found by computing the time derivative of the thermal energy caused by irreversible heating terms due to viscosity and shocks. We find that it is dominated by regions close the accretion radius R_{acc} . The energy dissipation rate rises rapidly from ~ 26 days, when accretion begins, until ~ 50 days after disruption, when it reaches a peak of $\sim 10^{44} \text{ erg s}^{-1}$ (roughly the Eddington limit). This is followed by a power-law decay that approximately matches the expected $t^{-5/3}$ energy dissipation from the mass fallback rate (Rees 1988; Phinney 1989) but with \dot{M}_{acc} lower than the mass fallback rate by approximately 2 orders of magnitude. We compare this to the luminosity derived from our measured mass accretion rate \dot{M} , given by $L_{\text{acc}} = \epsilon \dot{M} c^2$. Here, $\epsilon = 0.2$ is the efficiency based on our inner accretion radius. However, since our R_{acc} is inside the last stable orbit, matter

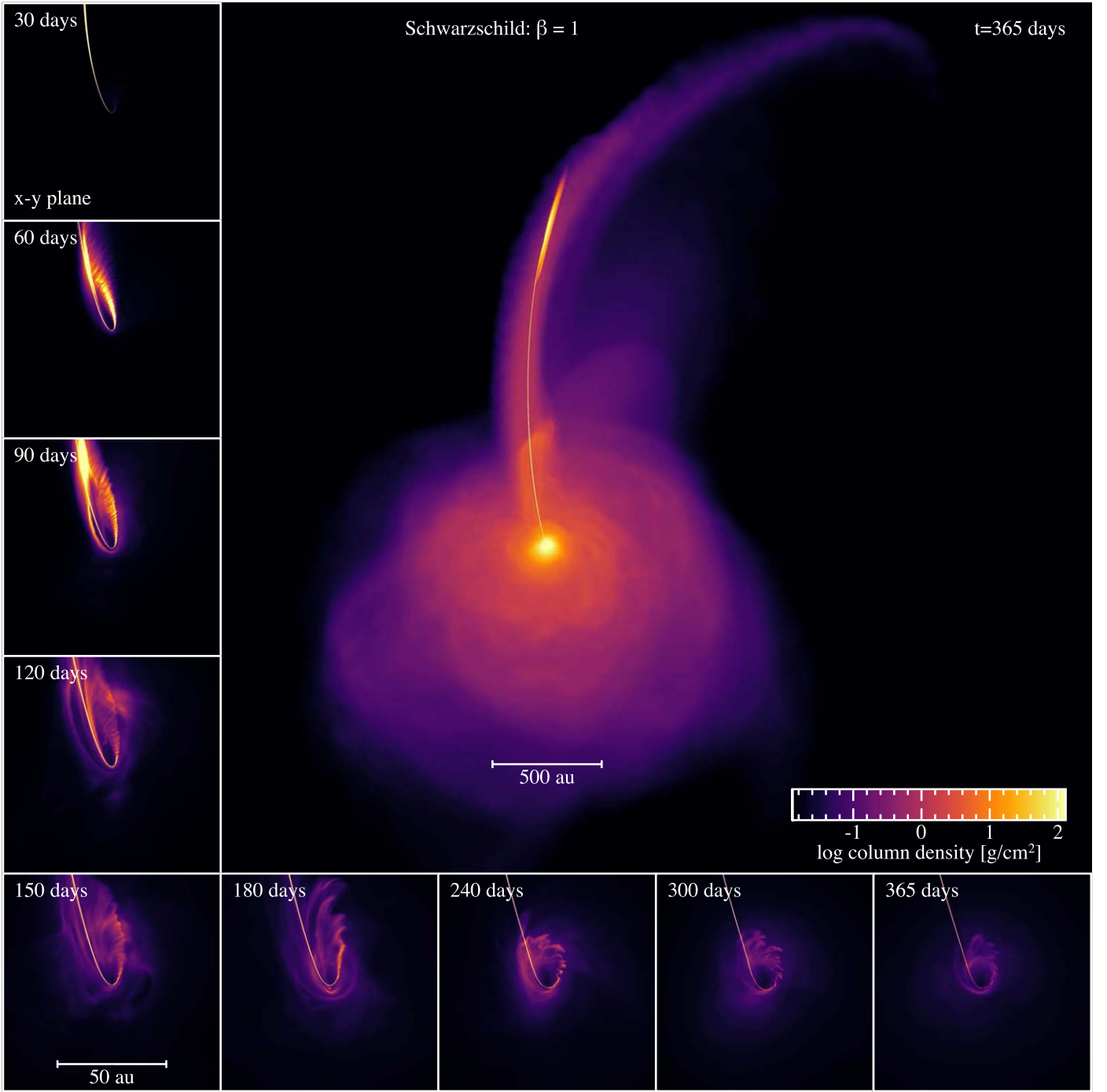


Figure 1. A year in the life of a TDE. We show snapshots of column density in the simulation of a $1 M_{\odot}$ star on a parabolic orbit with $\beta = 1$, disrupted by a $10^6 M_{\odot}$ black hole, using 4×10^6 SPH particles in the Schwarzschild metric. The main panel shows the large-scale outflows after 365 days projected in the x - y plane with log scale. Inset panels show the stream evolution on small scales (100×100 au), showing snapshots of column density projected in the x - y plane on a linear scale from 0 to 1500 g cm^{-2} (colors are allowed to saturate). The animation runs from 0 to 366 days. The real-time duration is 160 s. Data and scripts used to create the figure are available on Zenodo: doi:[10.5281/zenodo.11438154](https://doi.org/10.5281/zenodo.11438154).
(An animation of this figure is available in the [online article](#).)

crossing this radius is mostly advected into the black hole rather than radiated, so converting it into a luminosity simply measures the amount of energy that would have been dissipated to reach this radius if all the matter were on a perfectly circular orbit. The resulting “luminosity” L_{acc} follows the same trend as the actual energy dissipation rate above but is ~ 0.5 –1 orders of

magnitude greater throughout the simulation. This suggests that some material is accreted almost radially, with little to no orbital energy dissipated before accretion (Svirski et al. 2017).

The bottom panel of Figure 3 shows the approximate time taken for photons to diffuse from near the black hole out to the photosphere radius, assuming the material remains static. We

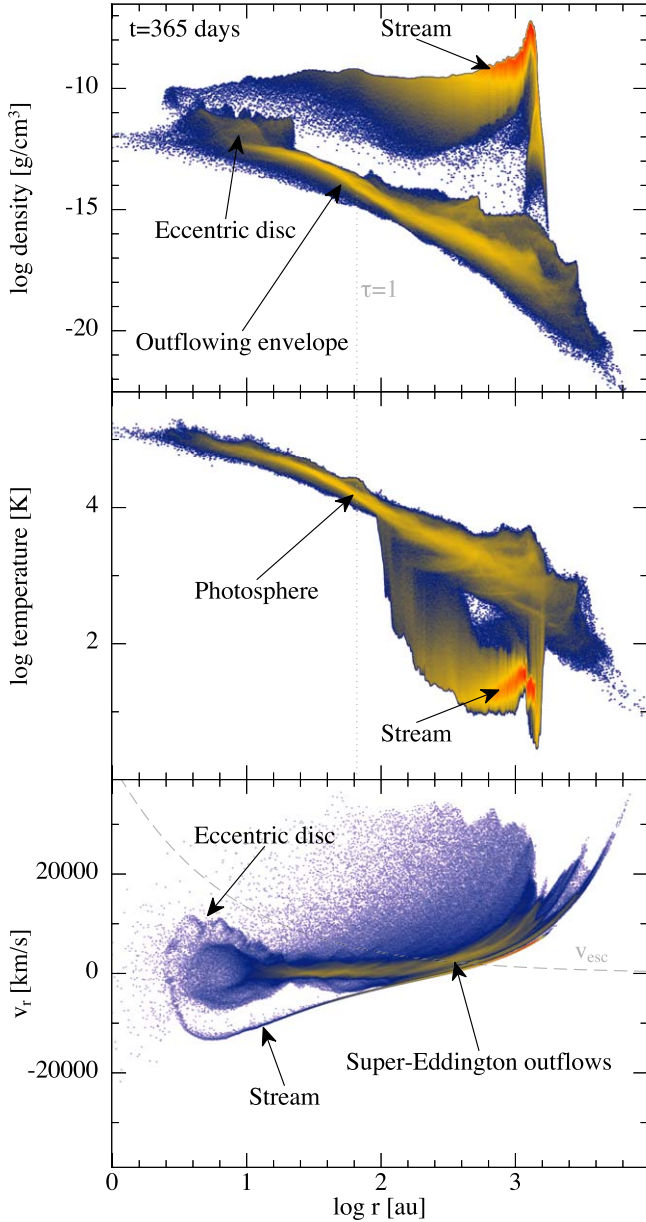


Figure 2. Distributions of density (top), temperature (middle), and radial velocity (bottom) at 1 yr postdisruption. Colors represent the density of points (mass per pixel) on the plot, with orange being a high density of points and blue being low. The dotted line indicates the $\tau = 1$ photosphere. The dashed line in the lower panel indicates $v_{\text{esc}} \equiv \sqrt{2GM_{\text{BH}}/r}$. All three distributions show features that may be identified as the high-density stream and the low-density, cool, expanding envelope. Typical outflow velocities are of order 10^4 km s^{-1} , similar to those measured in observed TDE spectra and the “mass-loaded outflows” predicted by Metzger & Stone (2016). The animation begins on day 0 and ends on day 366. The real-time duration of the animation is 64 s. Data and scripts used to create the figure are available on Zenodo: doi:10.5281/zenodo.11438154.

(An animation of this figure is available in the [online article](#).)

computed this via

$$\tau_{\text{diffuse}} \sim \frac{1}{c} \int_0^{R_{\text{photo}}} \kappa r \rho dr \quad (6)$$

by summing the contributions from each SPH particle intersecting a line of sight along each coordinate axis with opacity $\kappa = 0.4 \text{ cm}^2 \text{ g}^{-1}$. The typical photon diffusion time varies between ~ 10 and 200 days, peaking approximately 80 days

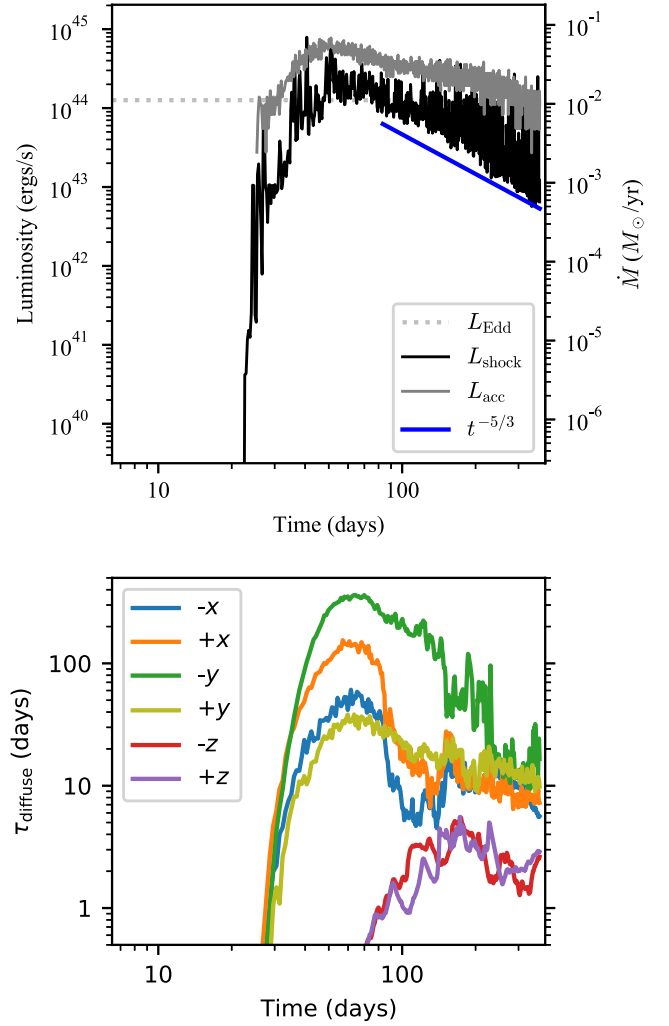


Figure 3. Top: energy dissipation rate and accretion luminosity evolution (from \dot{M} ; see right axis) compared to the Eddington luminosity and a $t^{-5/3}$ slope. Bottom: estimated photon diffusion timescale along different lines of sight (see legend). Data and scripts used to create the figure are available on Zenodo: doi:10.5281/zenodo.11438154.

after disruption and decaying roughly as a power law. This indicates that, although most energy is dissipated in regions close to the black hole (see Appendix B), where the reservoir of gravitational binding energy is largest, this material is optically thick. The energy is transported outward by mechanical outflows before some of it is radiated through a photosphere.

Figure 4 shows the temperature at the “photosphere” of the outflowing envelope, produced by ray-tracing through our simulation as described in Section 2.1. An expanding emission region of 10–100 au is consistent with those inferred from TDE observations (van Velzen et al. 2021). Photospheric temperatures are in the range expected to produce blackbody emission at UV/optical wavelength. Figure 2 shows that temperatures would remain in the 10^4 – 10^5 K range even accounting for scattering from deeper layers (see Appendix C).

Figure 5 compares the corresponding time evolution of our measured L_{bb} , R_{photo} , and T_{bb} (inferred bolometric luminosity, blackbody radius, and temperature of the blackbody fit to optical wavelengths, respectively) from six different lines of sight (solid lines) to the evolution of observed TDEs inferred from blackbody fits taken from Neustadt et al. (2020) and van

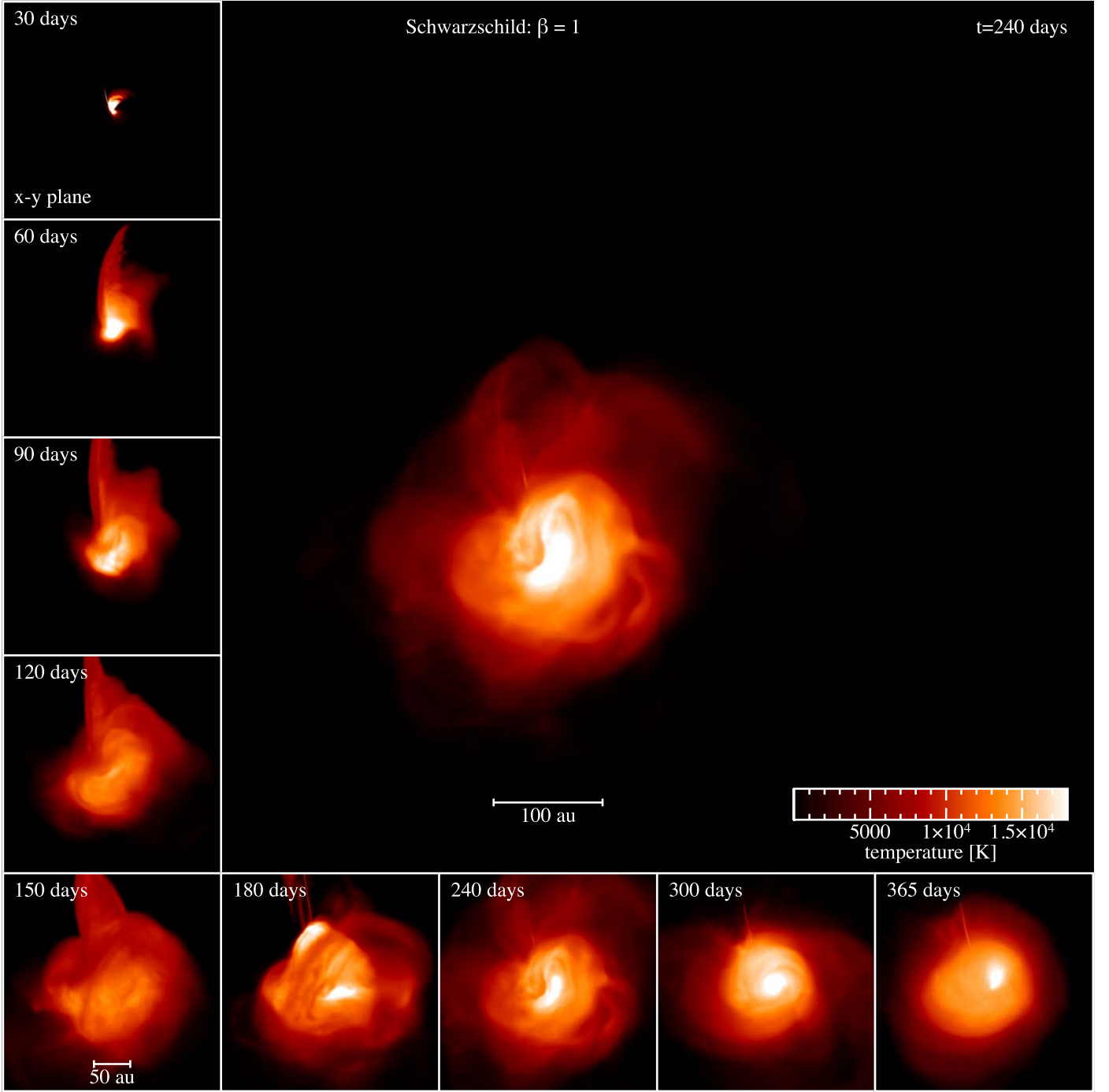


Figure 4. The Eddington envelope. We show the temperature at the photosphere for the simulation snapshots shown in Figure 1. The inner engine is obscured by the optically thick envelope. Temperatures correspond to thermal blackbody emission at UV/optical wavelengths. The animation shows the log density and temperature evolution at the photosphere on the left and right sides, respectively. The sequence begins on day 0 and ends on day 366. The real-time duration of the animation is 16 s. Data and scripts used to create the figure are available on Zenodo: doi:[10.5281/zenodo.11438154](https://doi.org/10.5281/zenodo.11438154).

(An animation of this figure is available in the [online article](#).)

Velzen et al. (2021; dots). The equivalent plot for the more penetrating $\beta = 5$ encounter is shown on the right.

The typical luminosity (top panel) is around 10^{43} – 10^{44} erg s $^{-1}$ ($10^{9.4}$ – $10^{10.4}$ L_{\odot}); however, we caution that the exact value is sensitive to our photospheric temperature (since $L \propto T^4$). Nonetheless, our approximate luminosities are consistent with the observed values (see Figure 9 of Holoien et al. 2019), as well as with the analytically computed lightcurves of Lodato & Rossi (2011; see left panel of their Figure 7). The bolometric

luminosity of the envelope in our models appears almost constant and close to the Eddington value, key features of the analytical model of Loeb & Ulmer (1997).

The photospheric radius (middle panels), when computed by fitting to synthetic spectra in the optical band (Appendix C), is relatively insensitive to the line of sight, giving typical radii of ~ 10 – 100 au (10^{14} – 10^{15} cm), in the same range as the observations. The photospheric radius reaches a peak after roughly 150–200 days in the $\beta = 1$ calculation and 50 days in

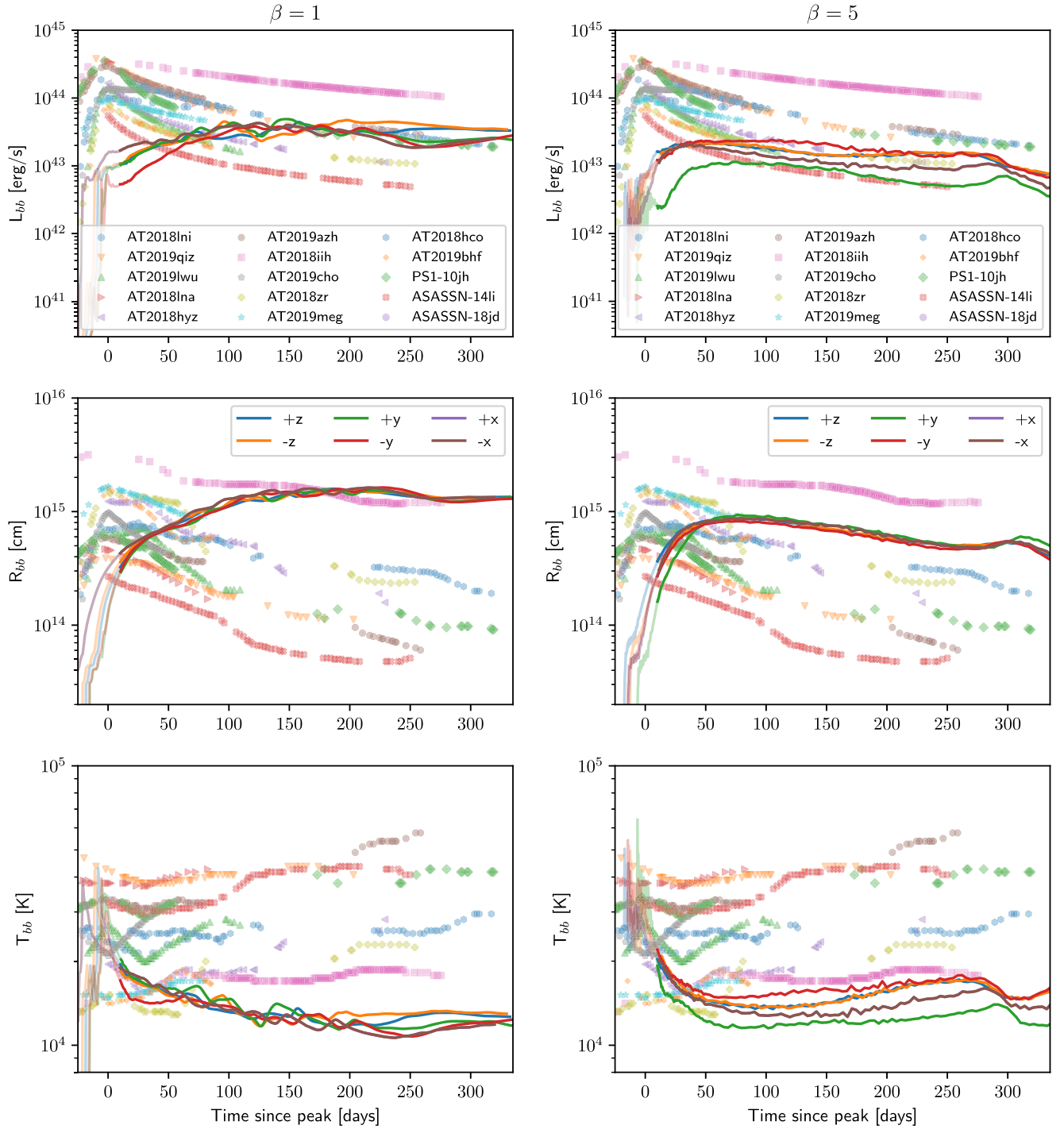


Figure 5. Optical luminosity (top), blackbody radius (middle), and temperature (bottom) evolution from our simulation using $\beta = 1$ (left) and $\beta = 5$ (right), measured along different lines of sight (see legend). Markers represent the fits to various observed TDEs taken from van Velzen et al. (2021) plus ASASSN-18jd (Neustadt et al. 2020). Transparency at $t \lesssim 30$ days indicates when the photosphere is unresolved. Data and scripts used to create the figure are available on Zenodo: doi:10.5281/zenodo.11438154.

the $\beta = 5$ calculation, the latter more closely matching the typical 20–50 day rise time seen in most of the observations. On the other hand, some TDE candidates, such as ASASSN-18jd (Neustadt et al. 2020; see legend), do show a more or less flat luminosity evolution over a 1 yr timescale, similar to our $\beta = 1$ lightcurves. The transients AT 2018hco and AT 2019iih show the closest match to the photospheric radius evolution in our $\beta = 5$ calculation, particularly for $t \gtrsim 50$ days.

We find photospheric temperatures (bottom panels) in the range of $1\text{--}4 \times 10^4$ K with the same range as the observations but slightly lower temperatures in our models ($T \sim 10^{4.1}$ K) compared to the observations ($T \sim 10^{4.2}\text{--}10^{4.6}$ K) for $t \gtrsim 50$ days. This may be a result of our underestimate of the photospheric temperature due to scattering of photons from deeper layers (Appendix C). The observed trend of temperatures slowly rising as a function of time for $t \gtrsim 50$ days is

reproduced in our $\beta = 5$ calculation (right panels of Figure 5). Our temperature evolution is similar to that obtained by Mockler et al. (2019), who fitted models of a “dynamic reprocessing layer” to observed TDEs (see their Figure 8), finding a 10–20 day sharp rise in temperature followed by a dip and subsequent flat or slowly rising evolution.

Notable features in both the $\beta = 1$ and $\beta = 5$ cases are the almost flat lightcurves predicted at late times along most lines of sight. This is also observed (e.g., Holoien et al. 2019; van Velzen et al. 2021). In our simulations, this corresponds to the stalling of the photospheric radii in an expanding gas cloud; however, as discussed below, models without cooling may not accurately describe lightcurves after ~ 1 yr.

4. Discussion

Our simulations address the main challenge of TDEs: to simulate the disruption of a $1 M_\odot$ star, on a parabolic orbit, by a $10^6 M_\odot$ black hole in general relativity and to model the subsequent accretion flow from first principles.

Our main new insight from doing so is that, as in Hu et al. (2024), we have been able to self-consistently form the hypothesized “Eddington envelope” for the first time, more or less as predicted by Loeb & Ulmer (1997) and Metzger & Stone (2016). With the disrupted star moving on an orbit with a mean energy of zero and low angular momentum, we found dissipation of energy and angular momentum to occur through relativistic precession and ensuing stream–stream collisions (see Appendix A), as found by previous authors for stars on bound trajectories (Bonnerot et al. 2016; Hayasaki et al. 2016; Liptai et al. 2019; Stone et al. 2019) and similar to the process originally envisioned by Rees (1988).

Once accretion commences in the optically thick environment with inefficient cooling (we assumed adiabatic gas), the gravitational energy of accreting material launches mechanical outflows, yielding a large, asymmetric, optically thick outflowing envelope (Figure 4).

We found a similar outflow in recent calculations of initially eccentric encounters (Hu et al. 2024) but with a faster rise of the lightcurve due to the shorter orbital periods. The main difference in the parabolic case is that only $\sim 1\%$ of the star is accreted, compared to more than half the star for the eccentric encounters (Hu et al. 2024). The lower efficiency of accretion occurs because of the smaller amount of bound material reaching the inner regions (Appendix A).

The envelope structure is similar to other rapidly expanding, optically thick, quasi-spherical outflows powered by a central energy source, such as supernovae and kilonovae. In this case, the expanding envelope is powered by gravitational energy, dissipated in the radiatively inefficient accretion flow onto the black hole (see Appendix B). Our black hole mass accretion rate, shown in Figure 3, is 1–1.5 orders of magnitude lower than the predicted mass fallback rate. This broad conclusion on the formation of an Eddington envelope is unchanged by whether or not the black hole is spinning or by whether the star approaches closer to the black hole (see Appendix D) or the numerical resolution (see Appendix E).

That our outflowing envelope, or “black hole Sun,” is optically thick is demonstrated by our estimated photon diffusion timescales of ~ 10 –100 days shown in the bottom panel of Figure 3. This means that the debris produced by the disruption cannot cool efficiently, leading to the formation of a photosphere. Synthetic spectral energy distributions

(Appendix C) show that this leads to ratios of optical to X-ray emission of order 10 – 10^3 , similar to those observed (van Velzen et al. 2021).

Our numerical experiments have several serious limitations in how well they represent real tidal disruptions. The main ones are that we employed an adiabatic approximation, meaning that none of the energy produced is actually radiated in our simulations, and that we assumed $\gamma = 5/3$ and used a polytrope, not a real star.

Our adiabatic assumption is likely a good approximation near the peak of the lightcurve since the photon diffusion timescale is long, although it does not account for the change to the radiation-pressure-dominated regime after shock heating, which implies that the adiabatic index should change to $4/3$. On the other hand, the adiabatic assumption likely breaks down by around 1 yr after disruption. At $t \gtrsim 1$ yr, our estimated luminosity (Figure 5) becomes comparable to the energy input rate from shock heating (Figure 3), while the photon diffusion timescale becomes comparable to the time for the kinetic outflows to reach the photosphere, allowing material to radiatively cool.

Therefore, at $t \gtrsim 1$ yr, with relatively efficient diffusion, the observable luminosity should transition to tracking the shock heating rate, which in turn roughly tracks the mass return rate with $\propto t^{-5/3}$ scaling (top panel of Figure 3). Efficient cooling after 1 yr may also lead to thin disk formation (see Appendix A), rather than the eccentric thick disk formed at $t \gtrsim 240$ days in Figure 1. Cooling may also cause our photospheres to retreat at later times, better matching the photospheric radius and temperature observations.

Despite this limitation, our photospheric radius estimates yield a luminosity evolution with the same order of magnitude as optical/UV lightcurves from several recently observed TDEs (see Figure 5). We do not expect that the dynamics of our simulations would be significantly affected by allowing the photosphere to radiate at early times, mainly because the energy release via radiation is small—most of the energy in our Eddington envelope is released via mechanical outflows, with typical outflow velocities of ~ 1 – 2×10^4 km s $^{-1}$ (see bottom panel of Figure 2). Such velocities match those observed in spectral lines (e.g., Leloudas et al. 2019).

We find that the optical lightcurve is sensitive to the observing angle, as suggested by Dai et al. (2018), but due to different photospheric temperatures along different lines of sight (see Figure 5) rather than the presence of a disk. Mildly supersonic outflows indicate that temperatures are not in equilibrium across the photosphere.

The photospheric radii plateau at ~ 20 –100 au, depending on the line of sight and the amount of material participating in the outflow (Figure 5). Applying a single-zone model with uniform density $\rho = \frac{4\pi M}{3 R^3}$ to a homologically expanding envelope, this stalling is estimated to occur when the photospheric radius is $\frac{2}{3} \sqrt{\frac{\kappa M}{4\pi}}$, where the mass M in the envelope depends on the penetration factor β . This estimate yields a photospheric radius plateau of ~ 100 au for our choice of κ and $M = 0.1 M_\odot$. While our predicted radius evolution might change if we allowed radiation to escape (especially at these late times), a significant late-time flattening has been observed in optical/UV for black holes of this mass (van Velzen et al. 2019).

Many TDE candidates show soft X-ray emission. While in general, the ratio of X-ray to optical luminosities in TDEs is low (Auchettl et al. 2017), there are cases where optical and

X-ray emission are both present. ASASSN-14li has similar X-ray and optical luminosities (Holoien et al. 2016), though with X-rays lagging by 32 days (Pasham et al. 2017), which is difficult to explain via reprocessing. Our model can help to explain some of these TDE features. At late times, as the material cools and the photosphere retreats to reveal regions close to the black hole, we expect the formation of a disk or a thick torus similar to that described in Appendix A, which will be a significant central X-ray source.

Indeed, we found in our $\beta = 5$ calculation (Appendix C) that the retreat of the photosphere produces a rising X-ray luminosity similar to some observed TDEs (Gezari et al. 2017) and to the class of “veiled” TDEs (Auchettl et al. 2017). Our Eddington envelope naturally obscures any central X-ray source, with absorption strongly varying for different lines of sight with typical $N_H \sim 10^{24} - 10^{26} \text{ cm}^{-2}$. This suggests an explanation for the dichotomy between X-ray and optical TDEs in terms of different viewing angles to the source in a sort of “unified” model for TDE emission (Dai et al. 2018).

5. Conclusions

In summary, we simulated the tidal disruption of $1 M_\odot$ polytropic stars around a $10^6 M_\odot$ black hole using general relativistic hydrodynamics in the Kerr metric, following the simulations for 1 yr postdisruption. Our main finding, similar to our recent finding for real stars on eccentric orbits (Hu et al. 2024), is the production of an optically thick “Eddington envelope” hypothesized by previous authors (e.g., Loeb & Ulmer 1997; Metzger & Stone 2016). Our calculations predict

1. outflow velocities of $\sim 10^4 \text{ km s}^{-1}$,
2. large photosphere radii of $\sim 10 - 100 \text{ au}$,
3. a relatively low mass accretion rate ($\sim 10^{-2} M_\odot \text{ yr}^{-1}$) mediated by the mechanical outflow of material, and
4. peak luminosities of $\sim 10^{43} - 10^{44} \text{ erg s}^{-1}$.

We find that our $\beta = 5$ encounters provide a better match to TDE observations than $\beta = 1$, and that black hole spin does not significantly change the outcome. We thus confirm Eddington envelopes as the likely solution to the puzzle of TDE optical/UV emission.

Acknowledgments

We thank the referee for constructive suggestions and Christophe Pinte, Benjamin Tessore, Sjoert Van Velzen, Nick Stone, Brian Metzger, Katie Auchettl, Matt Nicholl, James Miller-Jones, Adelle Goodwin, Jane Dai, Kate Alexander, Paul Lasky, Elli Borchert, Alex Heger, Brenna Mockler, Selma de Mink, Nathaniel Roth, Greg Salvesen, Eliot Quataert, and Bernhard Mueller for stimulating discussions. Thanks to Sjoert and Katie in particular for kindly sharing observational data. D.L. was funded through the Australian government Research Training Program. D.J.P. and I.M. are grateful for Australian Research Council funding via FT130100034 and FT190100574, respectively. This project received funding from the EU’s Horizon 2020 research and innovation program under the Marie Skłodowska-Curie grant 823823 (Dustbusters RISE project). Research at the Flatiron Institute was supported by the Simons Foundation. D.J.P. thanks them for expenses during his visit. This research was supported by grant NSF PHY-2309135 to the Kavli Institute for Theoretical Physics (KITP). We

acknowledge CPU time on OzSTAR funded by Swinburne University and the Australian Government.

Facility: OzSTAR

Software: PHANTOM (Price et al. 2018), SPLASH (Price 2007), MATPLOTLIB (Hunter 2007), SCIPY (Virtanen et al 2020)

Appendix A Radiatively Efficient Cooling and Disk Formation

Figure 6 demonstrates that disk formation can occur more rapidly if the gas is allowed to cool. We performed a medium-resolution simulation with the same parameters as in Figure 1 but using an isentropic approximation in which we discard all irreversible heating due to viscosity and shocks but retain heating and cooling due to PdV work; see Liptai et al. (2019). This shows that a compact, circularized disk can more efficiently form if the stream remains cold. The formation process is similar to the stream–stream collisions seen in simulations of tidally disrupted stars on bound orbits (Bonnerot et al. 2016; Hayasaki et al. 2016) caused by the general relativistic orbital precession (Rees 1988), except that the collisions occur at relatively large distances from the black hole (\sim tens of au) for our $\beta = 1$ encounter. No optically thick envelope is formed in the isentropic case, as the main energy source is switched off.

The second panel of Figure 6 quantifies the degree of relativistic apsidal precession, plotting three sample trajectories computed by integrating the geodesic equations⁷ for three sample particles in the returning debris stream with $a = 0$ (solid lines), which may be compared to the corresponding Newtonian trajectories (dashed lines). The relativistic precession, while small for $\beta = 1$, nevertheless leads to self-intersection of the stream and hence disk formation.

Figure 7 shows the same calculation but performed with a spinning black hole ($a = 0.99$; $\theta = 60^\circ$). The disk formation process can be seen to occur in a similar manner. The second panel shows the same set of orbital trajectories as in Figure 6 but computed with $a = 0.99$. These are indistinguishable from those shown in Figure 6, indicating that the spin does not play a large role in the disk formation process for $\beta = 1$ encounters. The main difference is that in the case of a spinning black hole, the disk that is subsequently formed undergoes differential Lense–Thirring precession leading to disk tearing as predicted by Nixon et al. (2012) and Nealon et al. (2015). Such differentially precessing rings are thought to be responsible for quasiperiodic oscillations in black hole accretion disks (Stella & Vietri 1998) and are also observed in TDEs (Pasham et al. 2019).

This approximation of efficient cooling throughout the disruption event is unrealistic. Hence, Figure 8 shows the results of an additional numerical experiment where we continued the medium-resolution adiabatic calculation (with the same parameters as Figure 1) but at 1 yr after disruption switched to an isentropic formulation. This corresponds to roughly the time when the photon diffusion time becomes short (Figure 3, bottom) and the adiabatic cooling rate exceeds the energy dissipation rate. However, in reality, the envelope would transition smoothly from nearly adiabatic expansion with inefficient cooling to efficient radiative cooling represented by the isentropic model. That we also form a circularized disk in this experiment (Figure 8) confirms that a disk would efficiently form even at low resolution if the material was allowed to cool.

⁷ <https://github.com/phantomSPH/phantom-geodesic>

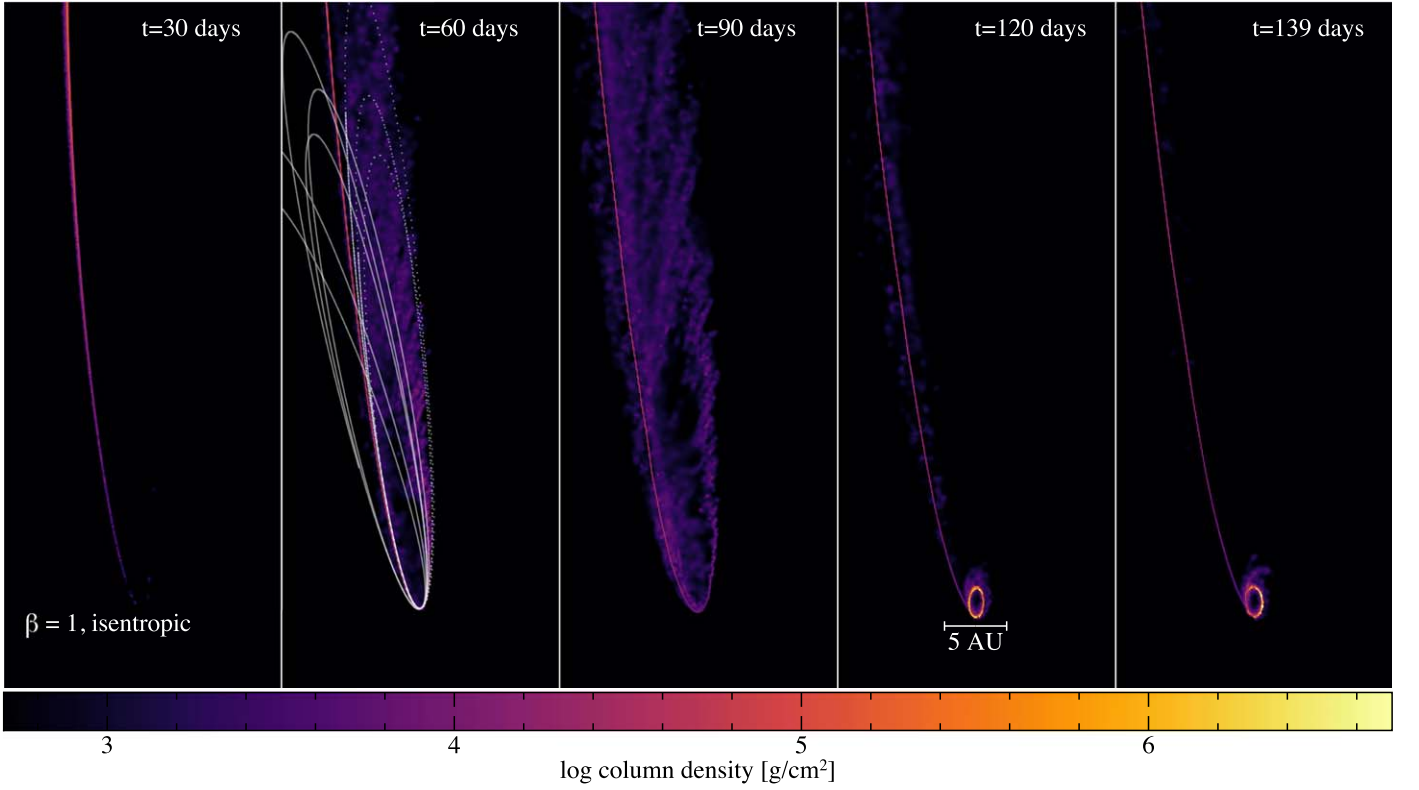


Figure 6. Disk formation in an isentropic simulation (radiatively efficient cooling) with a nonspinning black hole, as in Figure 1. After ~ 120 days, a narrow, circular ring of material forms in the orbital plane. In the second panel, we show the ballistic trajectories of three selected particles in the debris stream (solid white lines), showing how relativistic orbital precession leads to repeated self-intersection of the stream and subsequent disk formation. Dashed white lines show the corresponding Newtonian trajectories (i.e., without relativistic precession). The view is inclined by 60° to match Figure 7. Data and scripts used to create the figure are available on Zenodo: doi:[10.5281/zenodo.11438154](https://doi.org/10.5281/zenodo.11438154).

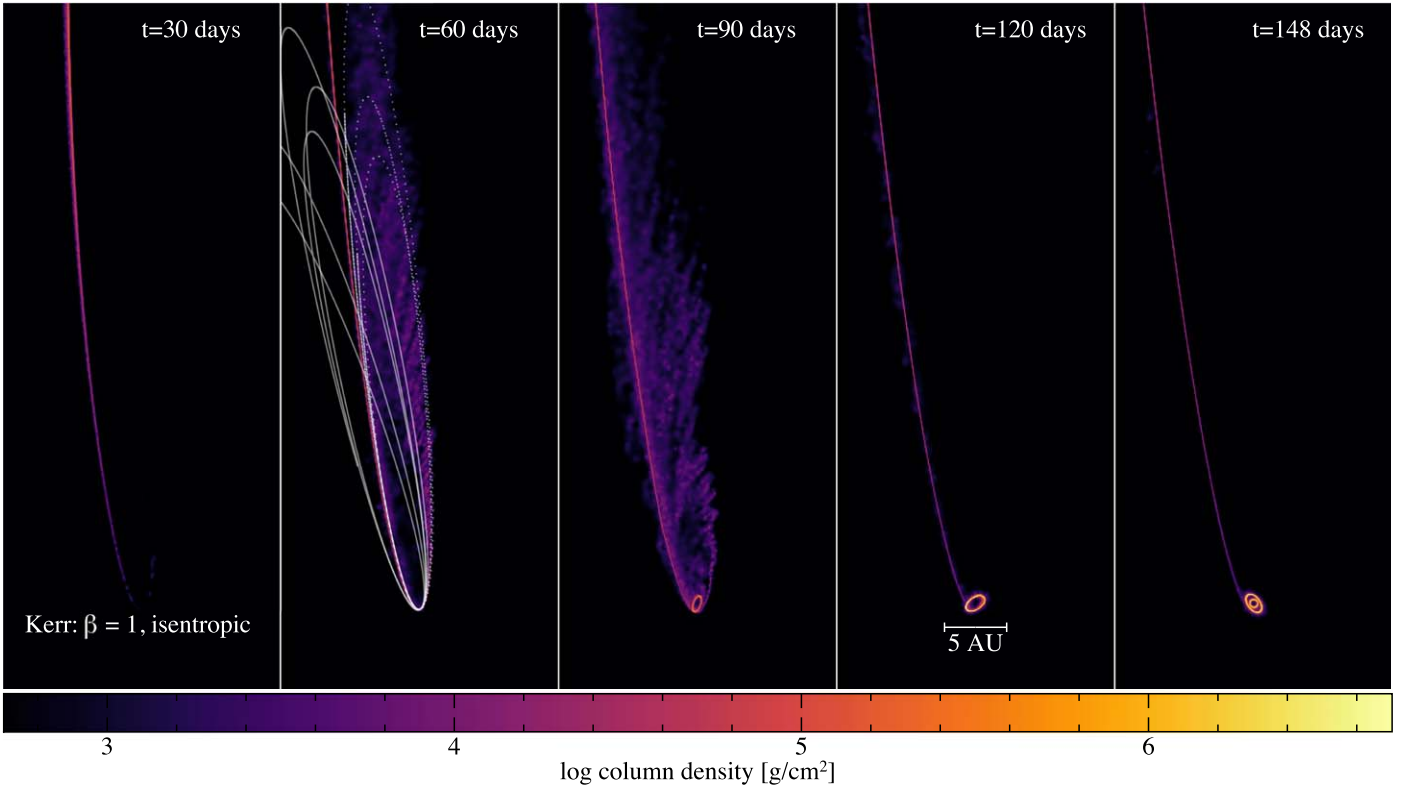


Figure 7. Disk formation in an isentropic simulation (radiatively efficient cooling) with a spinning black hole ($a = 0.99$, $\theta = 60^\circ$). The disk in this case is formed after 90 days and undergoes differential precession, which “tears” the disk into independent rings. Data and scripts used to create the figure are available on Zenodo: doi:[10.5281/zenodo.11438154](https://doi.org/10.5281/zenodo.11438154).

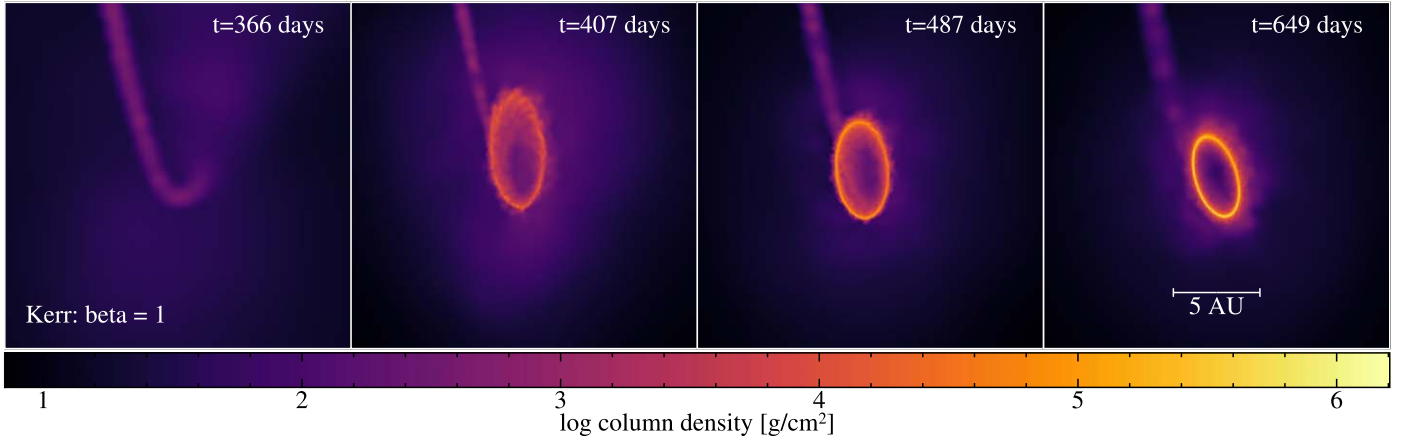


Figure 8. Disk formation in the core of the envelope when an adiabatic simulation is continued with radiatively efficient cooling. We resumed an adiabatic calculation (as in Figure 1) 1 yr after disruption assuming isentropic evolution. A narrow ring of material develops, similar to that obtained in the fully isentropic calculation (Figure 6). Each panel is 20 au \times 20 au.

Appendix B Thermodynamics

Our adiabatic simulations show lateral expansion of the stream in the nozzle shock that occurs during the second periapsis passage compared to isentropic calculations. Material in the returning stream, with a narrow range of energies and angular momenta, is spread out along a range of trajectories because of heating through the nozzle shock. Some of the nozzle shock heating is overestimated, especially at low numerical resolution (see Appendix E). However, provided the Mach number remains high, material continues to follow the precessing geodesic orbits similar to those shown in Figure 6. Figure 9 shows the line-of-sight averaged internal energy in our highest-resolution $\beta=1$ calculation (as shown in Figure 1). As the right panel of Figure 9 shows, the Mach number drops to around 50 after the nozzle shock in our highest-resolution calculation, which is sufficient to continue mostly along a geodesic trajectory.

More important to the circularization process is the “outer shock” due to self-intersection of the stream near apoapsis, labeled as “stream–stream collision” in the figure. Here, the Mach number drops to approximately unity in the shocked material (see right panel of Figure 9). Such material is then sprayed on a broad range of trajectories (as Appendix E), in particular providing the “cold accretion flow” (see labels in Figure 9) toward the black hole, enabling prompt accretion, similar to the process envisioned by Bonnerot & Lu (2020).

The process of stream–stream collisions initiating the accretion flow toward the black hole is similar to that which occurs in isentropic calculations (Appendix A). The main difference in the adiabatic simulations is that material reaching the inner regions close to the black hole no longer remains cold, with the additional heating producing kinetic outflows (Figure 9).

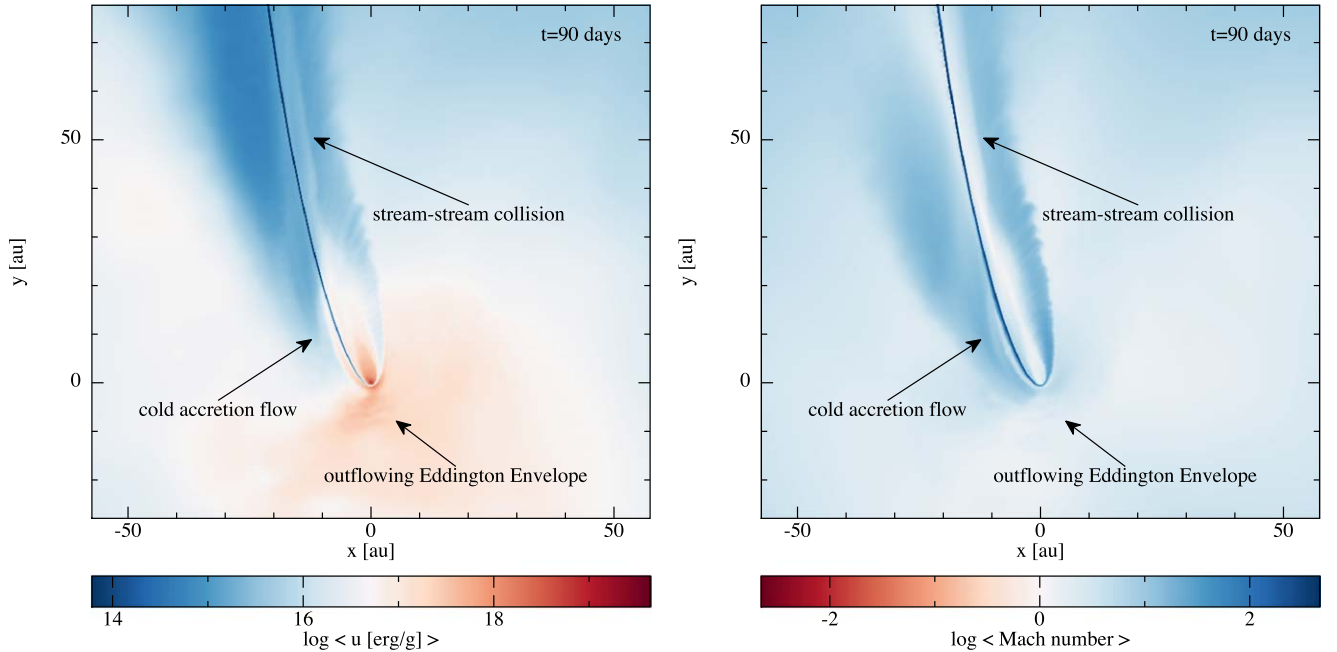


Figure 9. Thermodynamics of the accretion flow, showing line-of-sight averaged internal energy $\langle u \rangle \equiv \int \rho u dz / \int \rho dz$ (left) and Mach number (right) in the adiabatic calculation from Figure 1 (with $\beta = 1$, $a = 0$). The stream itself remains cold apart from mild heating caused by the nozzle shock at pericenter passage and some shock heating caused by stream–stream collisions near apocenter. The outflowing Eddington envelope is powered by the accretion flow toward the innermost regions near the black hole. Data and scripts used to create the figure are available on Zenodo: doi:[10.5281/zenodo.11438154](https://doi.org/10.5281/zenodo.11438154).

Appendix C Photospheric Evolution

Figure 10 shows our synthetic spectral energy distributions at selected times (see legend) for the $\beta = 1$ calculation. The overall spectrum is nonthermal, with significant excess at high energies compared to the optical blackbody fit (orange dotted curve; computed by fitting a single-temperature blackbody to the optical band using `scipy.optimize.curve\inferior fit`). The high-energy excess can be seen to produce soft X-rays whenever emission from the inner regions is visible. In the $\beta = 1$ calculation, this occurs for $t \lesssim 61$ days, before the Eddington envelope smothers the central engine (see corresponding panels in Figure 4).

While our predicted ratios of optical to X-ray emission of $1\text{--}10^3$ are similar to those observed, we find that our predicted X-ray emission depends on β . Observations also show slightly higher X-ray temperatures in the range $0.05\text{--}0.15$ keV (van Velzen et al. 2021) and tend to find X-ray luminosities that increase with time. Figure 11 shows that something close to this occurs for the $\beta = 5$ calculation. Here the more extreme precession leads to rapid smothering of the central engine in $t \lesssim 30$ days, but the faster stream dynamics means that the photosphere undergoes a visible retreat at $t \gtrsim 240$ days (see Figure 5) leading to increasing X-ray emission for $t \gtrsim 240$ days in the case where the star penetrates deeper.

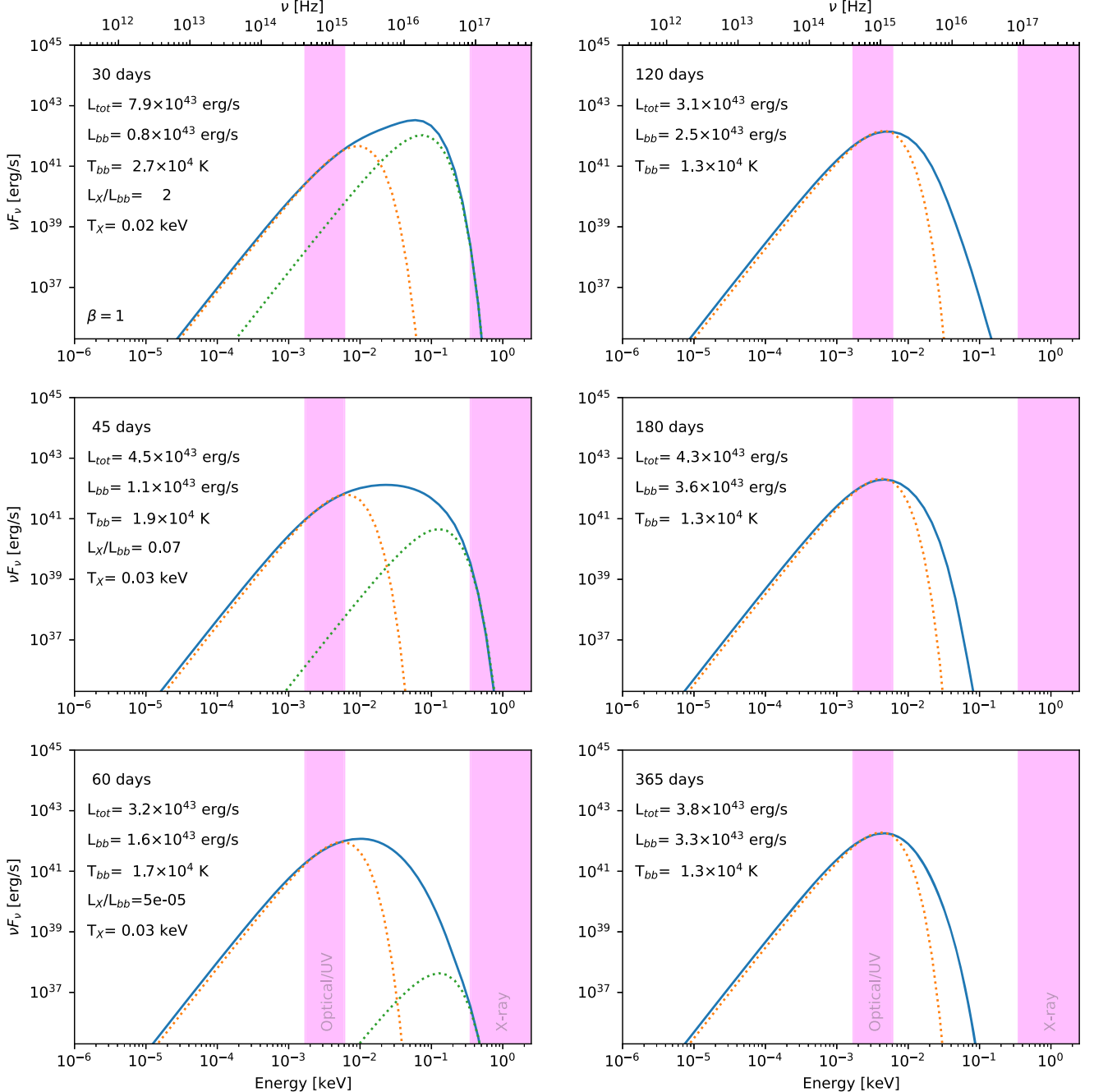


Figure 10. Synthetic spectral energy distributions computed from the $\beta = 1$ calculation with the observer in the $+z$ -direction (blue curves). Orange dotted curves show single-temperature blackbody fits to the optical band, while green dotted curves show blackbody fits to the soft X-ray band. The legend lists the luminosities (L_{tot} , L_{bb} , and L_x), the optical blackbody temperature (T_{bb}), and the X-ray temperature. Data and scripts used to create the figure are available on Zenodo: doi:10.5281/zenodo.11438154.

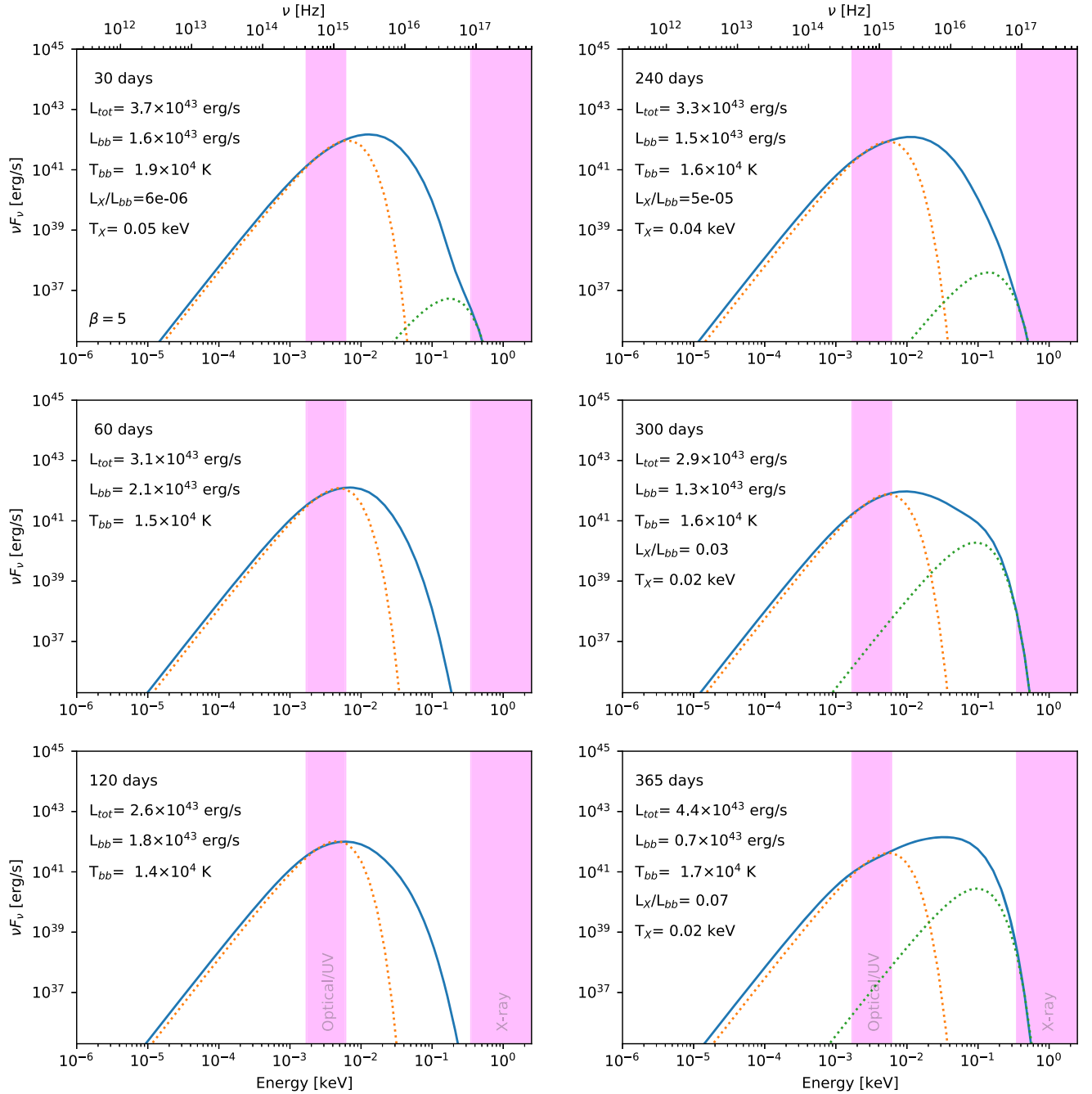


Figure 11. As in Figure 10 but for the $\beta = 5$ calculation. Here the “bubble” is inflated on a shorter timescale, smothering the central engine in $t < 30$ days, but the retreat of the photosphere at $t \gtrsim 240$ days leads to soft X-ray emission as the hotter central regions become visible. Data and scripts used to create the figure are available on Zenodo: doi:[10.5281/zenodo.11438154](https://doi.org/10.5281/zenodo.11438154).

Appendix D Effect of Penetration Factor

Figure 12 shows snapshots of the debris fallback for a calculation with an increased penetration factor of $\beta = 5$ for a Kerr black hole with $a = 0.99$ with the initial orbit inclined by 60° with respect to the black hole spin plane.

Since the star approaches much closer to the black hole, the effects of apsidal and Lense–Thirring precession throw the star/debris stream into an orbital plane that is different from the initial one. This changes the debris geometry projected in each

coordinate plane; however, the overall picture remains unchanged. That is, the returning debris stream feeds the expansion of a low-density Eddington envelope as in the $\beta = 1$ case. Circularization of the debris stream is faster in our $\beta = 5$ calculation because of the enhanced general relativistic precession, resulting in more prompt envelope formation (Figure 12).

The right panel of Figure 5 shows the corresponding lightcurves for this calculation (discussed in the main text), while Figure 11 shows the corresponding spectral energy distributions.

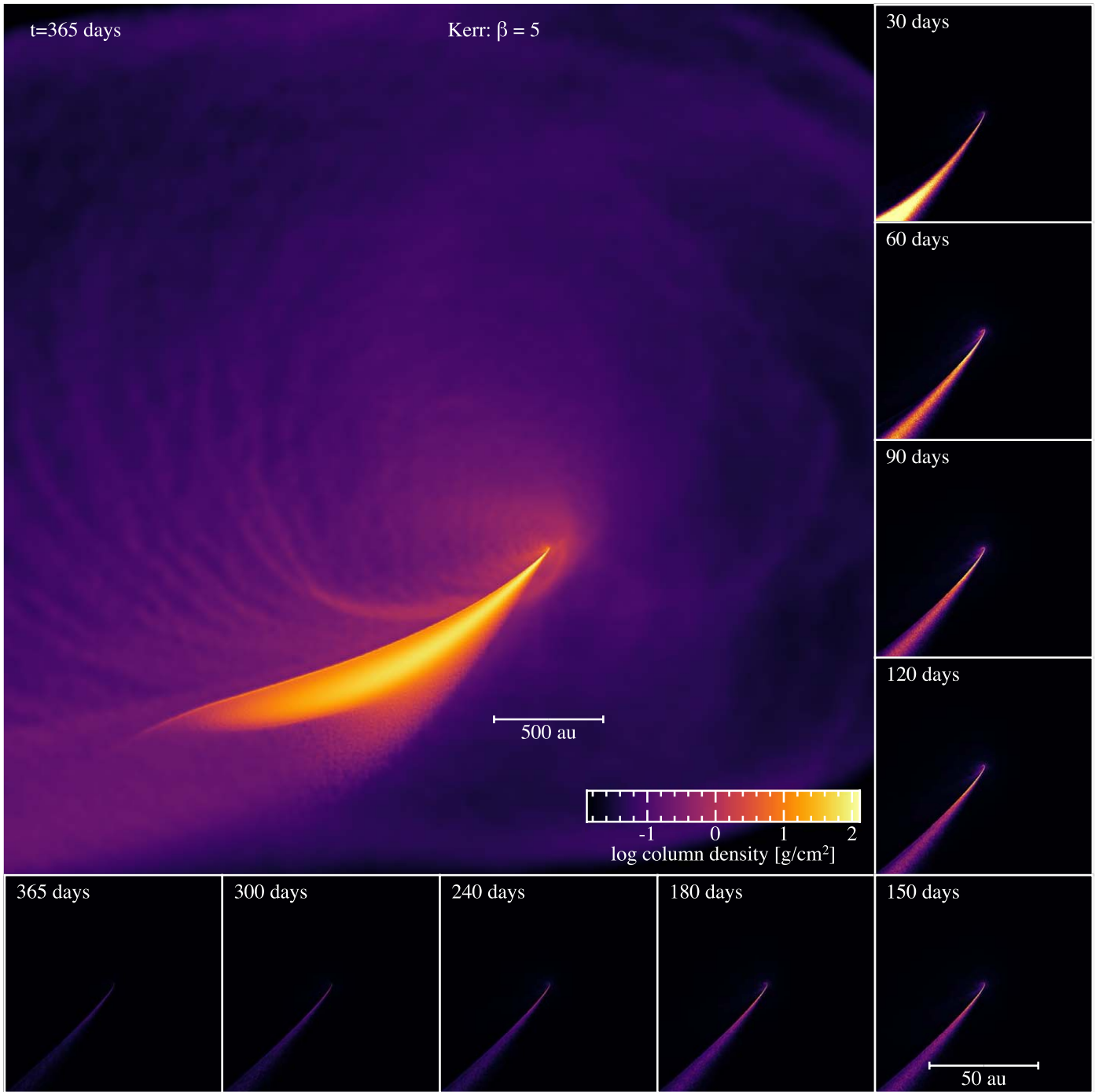


Figure 12. As in Figure 1 but for a star plunging closer to the black hole ($\beta = 5$). We show column density evolution for a $1 M_{\odot}$ star on a parabolic orbit with $\beta = 5$, disrupted by a $10^6 M_{\odot}$ Kerr black hole with spin $a = 0.99$. The initial orbital plane is misaligned by 60° to the black hole spin plane. The main panel shows the debris after 365 days projected in the x - y plane with a log color bar. Inset panels show stream evolution with a linear color bar between 0 and 1500 g cm^{-2} . Data and scripts used to create the figure are available on Zenodo: doi:[10.5281/zenodo.11438154](https://doi.org/10.5281/zenodo.11438154).

Appendix E Effect of Resolution

Figure 13 shows the effect of resolution in our simulations. The setup is identical to that shown in Figure 1. The top row compares the large-scale structure, while the bottom row compares the details of the stream on a smaller scale as it passes through the nozzle shock. We increased the number of particles by approximately a factor of 8 between each column

from left to right, corresponding to a factor of 2 increase in spatial resolution. We find that heating through the nozzle shock is overestimated at low numerical resolutions, leading to a more isotropic outflow. While the degree of nozzle shock heating is not fully converged even at our highest resolution (as expected from Bonnerot & Lu 2022), the Mach number remains sufficiently high that the material mostly follows colder trajectories along orbital geodesics as in the isentropic case (see Figure 6). Hence, the process of circularization tends

t=55 days

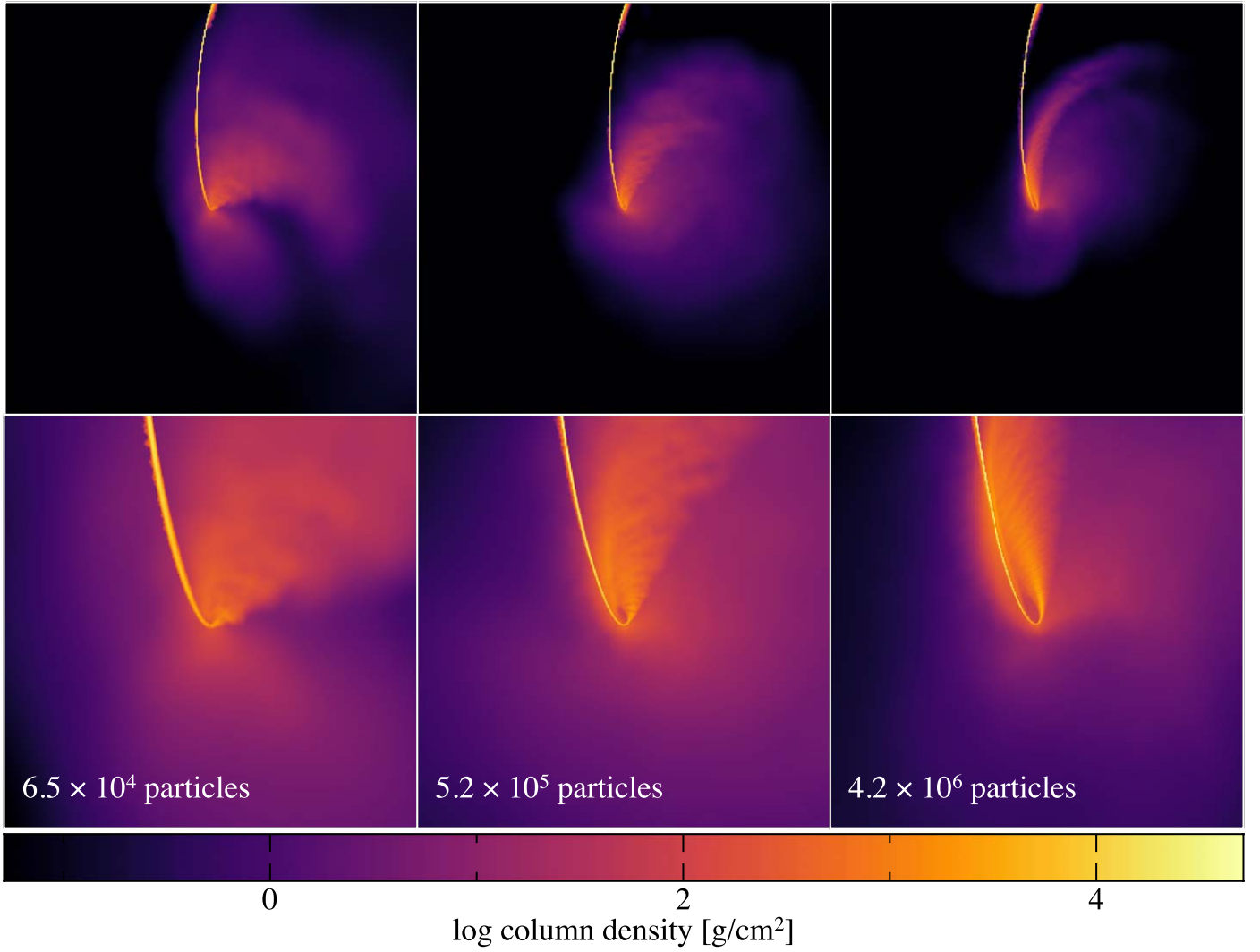


Figure 13. Effect of resolution in calculations with $a = \theta = 0$ and $\beta = 1$, as in Figure 1. Top row: comparison of the large-scale structure, where each panel is $500 \text{ au} \times 500 \text{ au}$. Bottom row: comparison of the stream fanning at small scales, where each panel is $100 \text{ au} \times 100 \text{ au}$. The total number of particles increases by approximately a factor of 8 between columns from left to right, with the third column corresponding to the resolution used in our main calculations. Data and scripts used to create the figure are available on Zenodo: doi:[10.5281/zenodo.11438154](https://doi.org/10.5281/zenodo.11438154).

toward being driven mainly by the stream self-intersection at apocenter rather than nozzle shock heating at pericenter, which is dominant at low resolution. Our results also imply that the envelope may be less isotropic in reality, with more material in a “spiral arm” that is denser than the rest of the envelope.

To clarify the numerical dependence of the lateral stream expansion in the nozzle shock, we performed two additional numerical experiments. The first involved a simple injection of material at different Mach numbers into an otherwise empty domain with no central black hole. We chose parameters typical of those observed in the tidal disruption calculations by injecting material in a stream at the typical location of the returning stream just prior to pericenter in our calculations, namely, at $(x, y) = (105, -150)$ in geometric units. We fixed the injection velocity to be the incoming stream velocity observed in our simulations, namely, at $v = 0.5\sqrt{GM/R_p}$, where R_p is the pericenter distance for the original star, at $R_p = R_t = 47.1 GM/c^2$. We injected a stream as a cylinder of particles with a radius of $10 R_\odot$ and varied the Mach number of the stream (by setting the incoming thermal energy u). Particles were

placed in a cubic lattice arrangement cropped to the radius of the cylinder. Calculations were performed with an adiabatic equation of state with $\gamma = 5/3$. We adopted a resolution of 16 particles per stream width, giving 565,940 particles in the domain at $t = 100$. The mass of the SPH particles is arbitrary for this problem (we chose $m_{\text{part}} = 10^{-12} M$), and we employed the nonrelativistic version of PHANTOM for simplicity.

Figure 14 shows the results of this experiment. The lateral expansion of the stream can be seen to be a simple function of the Mach number of the flow. Below Mach 10, significant lateral expansion of the stream may be observed. We found the degree of lateral expansion to be independent of both the injected stream width and the numerical resolution, depending solely on the Mach number.

Our second experiment (Figure 15) was the same but with a point mass placed at the origin with $M = M_{\text{BH}} = 10^6 M_\odot$ to capture the pericenter dynamics. Since we injected material with a finite width but a single velocity, the infinite Mach number orbital trajectories of the highly eccentric orbits cause a “traffic jam” at pericenter, which induces PdV work on the

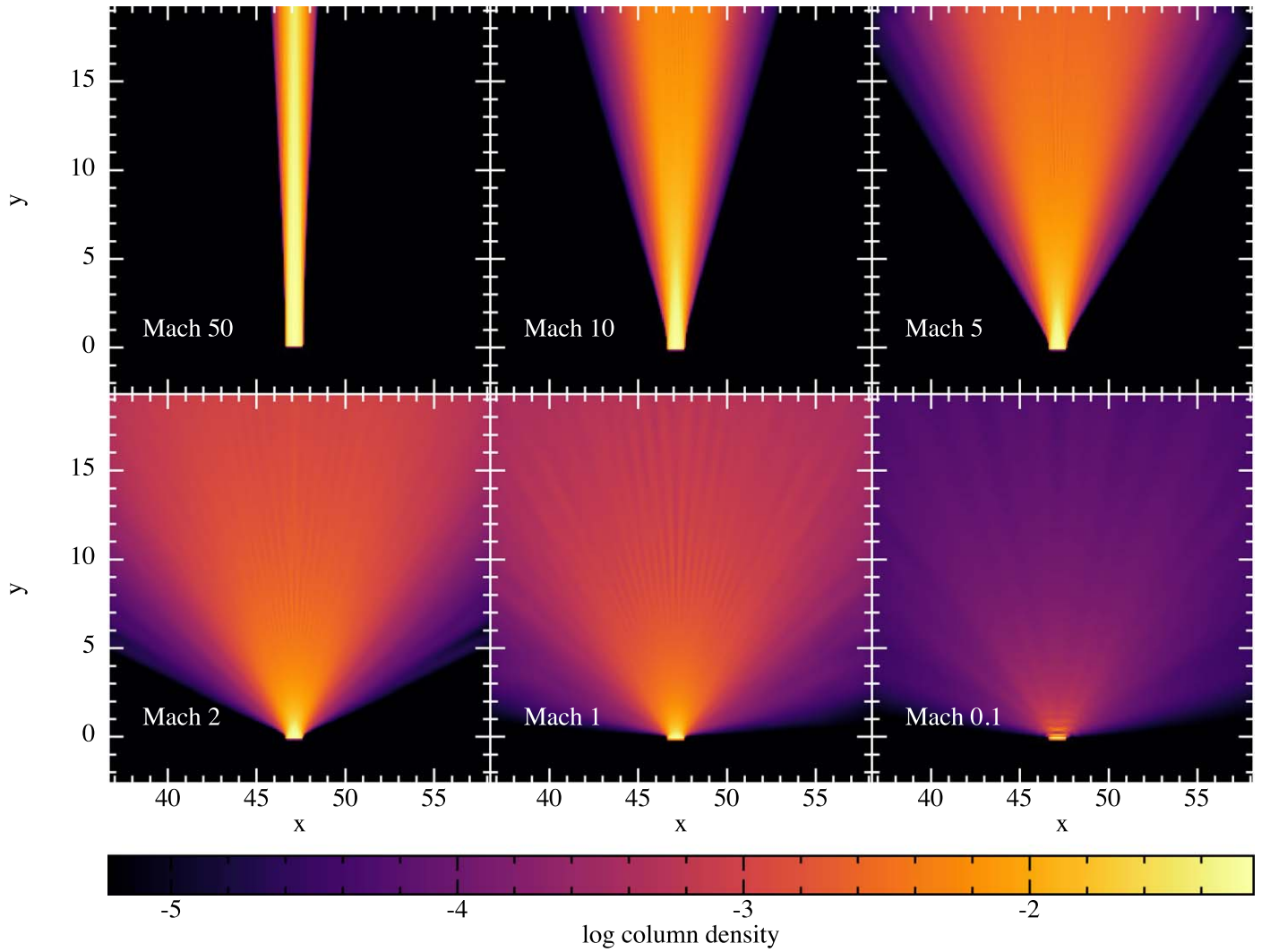


Figure 14. Numerical experiment where a stream is injected into an otherwise empty domain with a fixed injection speed but varying Mach numbers. Lateral expansion of the stream can be seen to depend solely on the Mach number of the flow. Data and scripts used to create the figure are available on Zenodo: doi:[10.5281/zenodo.11438154](https://doi.org/10.5281/zenodo.11438154).

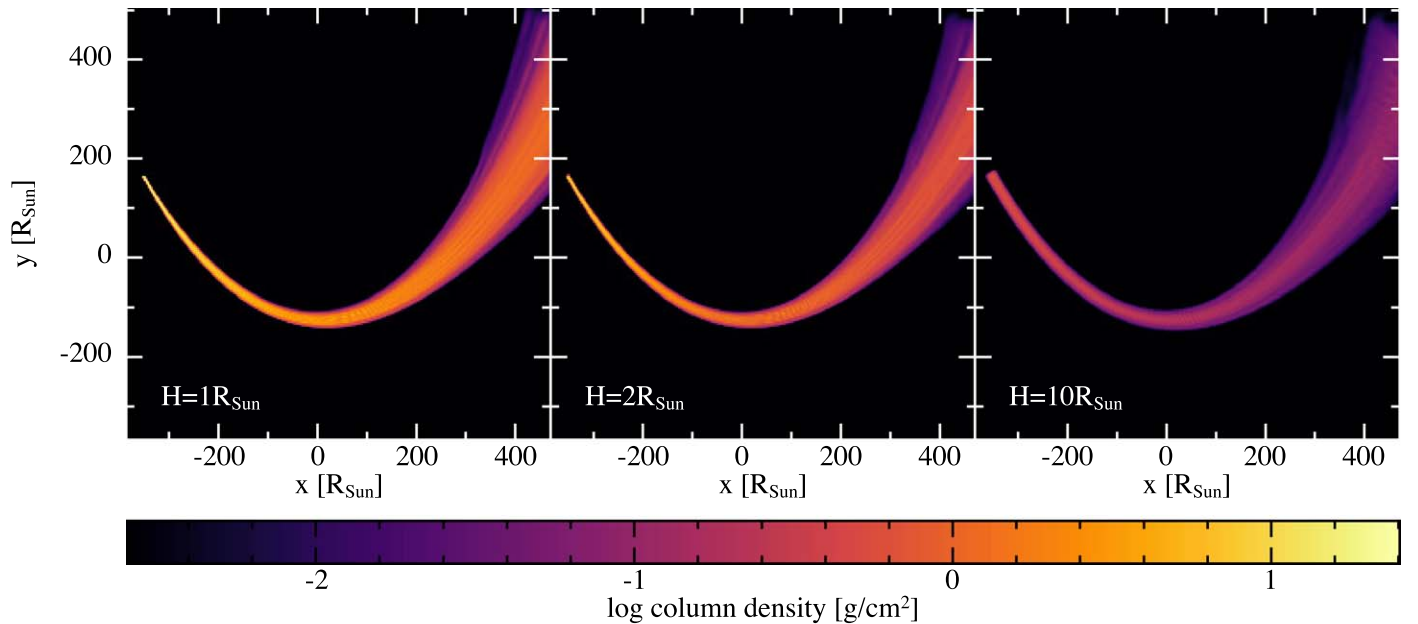


Figure 15. As in Figure 14 but with a point mass placed at the origin and experimenting with different initial stream radii H for the same initial Mach number of $M = 50$. Data and scripts used to create the figure are available on Zenodo: doi:[10.5281/zenodo.11438154](https://doi.org/10.5281/zenodo.11438154).

stream. We adopted an initial Mach number of 50, consistent with that measured from our tidal disruption calculations, but set the initial radius of the injected stream to $R = 1, 2$, and $10 R_{\odot}$, respectively. Apart from the overall drop in density as the stream width is increased, the lateral expansion of the stream remained the same in all cases. This demonstrates that an artificially wide or unresolved stream width is not the main cause of the lateral expansion.

Figure 13 shows that the postpericenter Mach number drop is overestimated at low resolution due to excess heating in the nozzle shock, leading to an overestimated stream width. The qualitative behavior is unchanged so long as the postpericenter Mach number remains high, as occurs in our highest-resolution adiabatic calculations and isentropic calculations at all resolutions.

Conservation properties are well preserved by the numerical scheme at all resolutions. For example, in the calculation shown in Figure 1, the energy error is $\Delta E/E \sim 6 \times 10^{-4}$ up to ~ 20 days when accretion commences, after which the total energy rises steadily due to the removal of accreted mass with negative specific energy from the simulation. Total angular momentum is conserved to $\Delta L/L \sim 2 \times 10^{-4}$ (0.02%) over the entire 365 days of the simulation.

ORCID iDs

Daniel J. Price  <https://orcid.org/0000-0002-4716-4235>
 David Liptai  <https://orcid.org/0000-0002-4856-1750>
 Ilya Mandel  <https://orcid.org/0000-0002-6134-8946>
 Joanna Shepherd  <https://orcid.org/0009-0005-3436-072X>
 Giuseppe Lodato  <https://orcid.org/0000-0002-2357-7692>
 Yuri Levin  <https://orcid.org/0000-0002-6987-1299>

References

- Abramowicz, M. A., Novikov, I. D., & Paczynski, B. 1991, *ApJ*, **369**, 175
 Andalmán, Z. L., Liska, M. T. P., Tchekhovskoy, A., Coughlin, E. R., & Stone, N. 2022, *MNRAS*, **510**, 1627
 Arcavi, I., Gal-Yam, A., Sullivan, M., et al. 2014, *ApJ*, **793**, 38
 Auchettl, K., Guillochon, J., & Ramirez-Ruiz, E. 2017, *ApJ*, **838**, 149
 Ayal, S., Livio, M., & Piran, T. 2000, *ApJ*, **545**, 772
 Bonnerot, C., & Lu, W. 2020, *MNRAS*, **495**, 1374
 Bonnerot, C., & Lu, W. 2022, *MNRAS*, **511**, 2147
 Bonnerot, C., Rossi, E. M., & Lodato, G. 2016, *MNRAS*, **458**, 3324
 Bonnerot, C., Rossi, E. M., Lodato, G., & Price, D. J. 2016, *MNRAS*, **455**, 2253
 Calderón, D., Pejcha, O., Metzger, B. D., & Duffell, P. C. 2024, *MNRAS*, **528**, 2568
 Chornock, R., Berger, E., Gezari, S., et al. 2014, *ApJ*, **780**, 44
 Coughlin, E. R., & Begelman, M. C. 2014, *ApJ*, **781**, 82
 Dai, L., McKinney, J. C., Roth, N., Ramirez-Ruiz, E., & Miller, M. C. 2018, *ApJL*, **859**, L20
 Diener, P., Frolov, V. P., Khokhlov, A. M., Novikov, I. D., & Pethick, C. J. 1997, *ApJ*, **479**, 164
 Evans, C. R., & Kochanek, C. S. 1989, *ApJL*, **346**, L13
 Frolov, V. P., Khokhlov, A. M., Novikov, I. D., & Pethick, C. J. 1994, *ApJ*, **432**, 680
 Gafton, E., & Rosswog, S. 2019, *MNRAS*, **487**, 4790
 Gezari, S., Cenko, S. B., & Arcavi, I. 2017, *ApJL*, **851**, L47
 Gezari, S., Chornock, R., Rest, A., et al. 2012, *Nature*, **485**, 217
 Goicovic, F. G., Springel, V., Ohlmann, S. T., & Pakmor, R. 2019, *MNRAS*, **487**, 981
 Golightly, E. C. A., Coughlin, E. R., & Nixon, C. J. 2019, *ApJ*, **872**, 163
 Guillochon, J., Manukian, H., & Ramirez-Ruiz, E. 2014, *ApJ*, **783**, 23
 Guillochon, J., & Ramirez-Ruiz, E. 2013, *ApJ*, **767**, 25
 Guillochon, J., Ramirez-Ruiz, E., Rosswog, S., & Kasen, D. 2009, *ApJ*, **705**, 844
 Hatfull, R. W. M., Ivanova, N., & Lombardi, J. C. 2021, *MNRAS*, **507**, 385
 Hayasaki, K., Stone, N., & Loeb, A. 2013, *MNRAS*, **434**, 909
 Hayasaki, K., Stone, N., & Loeb, A. 2016, *MNRAS*, **461**, 3760
 Holoien, T. W. S., Kochanek, C. S., Prieto, J. L., et al. 2016, *MNRAS*, **455**, 2918
 Holoien, T. W. S., Huber, M. E., Shappee, B. J., et al. 2019, *ApJ*, **880**, 120
 Hu, F. F., Price, D. J., & Mandel, I. 2024, *ApJL*, **963**, L27
 Huang, X., Davis, S. W., & Jiang, Y.-f. 2023, *ApJ*, **953**, 117
 Hunter, J. D. 2007, *CSE*, **9**, 90
 Jiang, Y.-F., Guillochon, J., & Loeb, A. 2016, *ApJ*, **830**, 125
 Kerr, R. P. 1963, *PhRvL*, **11**, 237
 Kesden, M. 2012, *PhRvD*, **86**, 064026
 Khokhlov, A., Novikov, I. D., & Pethick, C. J. 1993, *ApJ*, **418**, 181
 Kobayashi, S., Laguna, P., Phinney, E. S., & Mészáros, P. 2004, *ApJ*, **615**, 855
 Laguna, P., Miller, W. A., & Zurek, W. H. 1993, *ApJ*, **404**, 678
 Law-Smith, J., Guillochon, J., & Ramirez-Ruiz, E. 2019, *ApJL*, **882**, L25
 Leloudas, G., Dai, L., Arcavi, I., et al. 2019, *ApJ*, **887**, 218
 Liptai, D., & Price, D. J. 2019, *MNRAS*, **485**, 819
 Liptai, D., Price, D. J., Mandel, I., & Lodato, G. 2019, arXiv:1910.10154
 Lodato, G. 2012, Tidal Disruption Events and AGN Outbursts, European Physical Journal Web of Conf., 39, ed. R. Saxton & S. Komossa, (Madrid: EDP Sciences), 01001
 Lodato, G., King, A. R., & Pringle, J. E. 2009, *MNRAS*, **392**, 332
 Lodato, G., & Rossi, E. M. 2011, *MNRAS*, **410**, 359
 Loeb, A., & Ulmer, A. 1997, *ApJ*, **489**, 573
 Matsumoto, T., & Metzger, B. D. 2022, *ApJ*, **938**, 5
 Metzger, B. D. 2022, *ApJL*, **937**, L12
 Metzger, B. D., & Stone, N. C. 2016, *MNRAS*, **461**, 948
 Miller, M. C. 2015, *ApJ*, **805**, 83
 Mockler, B., Guillochon, J., & Ramirez-Ruiz, E. 2019, *ApJ*, **872**, 151
 Nealon, R., Price, D. J., & Nixon, C. J. 2015, *MNRAS*, **448**, 1526
 Neustadt, J. M. M., Holoien, T. W. S., Kochanek, C. S., et al. 2020, *MNRAS*, **494**, 2538
 Nicholl, M., Blanchard, P. K., Berger, E., et al. 2019, *MNRAS*, **488**, 1878
 Nixon, C., King, A., Price, D., & Frank, J. 2012, *ApJL*, **757**, L24
 Ogura, K., & Fukue, J. 2013, *PASJ*, **65**, 92
 Pasham, D. R., Cenko, S. B., Sadowski, A., et al. 2017, *ApJL*, **837**, L30
 Pasham, D. R., Remillard, R. A., Fragile, P. C., et al. 2019, *Sci*, **363**, 531
 Patra, K. C., Lu, W., Brink, T. G., et al. 2022, *MNRAS*, **515**, 138
 Phinney, E. S. 1989, in IAU Symp. 136, The Center of the Galaxy, ed. M. Morris (Dordrecht: Kluwer), 543
 Piran, T., Svirski, G., Krolik, J., Cheng, R. M., & Shiokawa, H. 2015, *ApJ*, **806**, 164
 Price, D. J. 2007, *PASA*, **24**, 159
 Price, D. J., Wurster, J., Tricco, T. S., et al. 2018, *PASA*, **35**, e031
 Ramirez-Ruiz, E., & Rosswog, S. 2009, *ApJL*, **697**, L77
 Rees, M. J. 1988, *Natur*, **333**, 523
 Rosswog, S., Ramirez-Ruiz, E., Hix, W. R., & Dan, M. 2008, *CoPhC*, **179**, 184
 Roth, N., Kasen, D., Guillochon, J., & Ramirez-Ruiz, E. 2016, *ApJ*, **827**, 3
 Ryu, T., Krolik, J., Piran, T., Noble, S. C., & Avara, M. 2023, *ApJ*, **957**, 12
 Sacchi, A., & Lodato, G. 2019, *MNRAS*, **486**, 1833
 Sadowski, A., Tejada, E., Gafton, E., Rosswog, S., & Abarca, D. 2016, *MNRAS*, **458**, 4250
 Steinberg, E., & Stone, N. C. 2024, *Natur*, **625**, 463
 Stella, L., & Vietri, M. 1998, *ApJL*, **492**, L59
 Stone, N. C., Kesden, M., Cheng, R. M., & van Velzen, S. 2019, *GRGr*, **51**, 30
 Strubbe, L. E., & Quataert, E. 2009, *MNRAS*, **400**, 2070
 Svirski, G., Piran, T., & Krolik, J. 2017, *MNRAS*, **467**, 1426
 Tejada, E., Gafton, E., Rosswog, S., & Miller, J. C. 2017, *MNRAS*, **469**, 4483
 van Velzen, S. 2018, *ApJ*, **852**, 72
 van Velzen, S., Stone, N. C., Metzger, B. D., et al. 2019, *ApJ*, **878**, 82
 van Velzen, S., Farrar, G. R., Gezari, S., et al. 2011, *ApJ*, **741**, 73
 van Velzen, S., Gezari, S., Hammerstein, E., et al. 2021, *ApJ*, **908**, 4
 Virtanen, P., Gommers, R., Oliphant, T. E., et al. 2020, *NatMe*, **17**, 261